Aptamer-Based Biosensor for Prostate Specific Antigen Detection Using Cobalt Phthalocyanine-Exfoliated Graphite Composites.

A thesis submitted in fulfilment of the requirements for the degree of

Masters in Chemistry

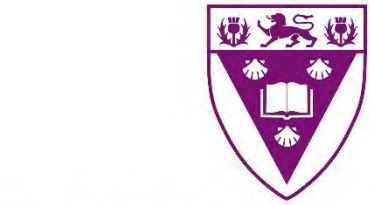

By

Emihle Benise

Supervisor: Dist. Professor T. Nyokong

Co-Supervisor: Dr J. Britton

November 2023

Dedication

I dedicate this work to my late grandparents; Noxolo Pegotty Benise and Nothemba Hermon Mfundisi, my slibings; Yonelisa, Solulele, Andonele, Inathi, Alunamda and Iphemna.

Acknowledgements

This work would have not been possible without the following:

My supervisor, Distinguished Professor Tebello Nyokong who believed in me, pushed me and made the MSc journey a success for me. I also acknowledge my mentor, Dr Lekhetho Mpeta for the guidance through my first year of this degree in which he helped me discovered a lot of things that helped in progressing this work. I extend my gratitude to Gail, Dr J Britton, Papa Francis, Prof J Mack, chemistry department and my s22 lab mates for the support that they gave me, physically and emotionally. To my family and friends, thank you for the support and encouragement. I am grateful to Rhodes University and Institute for Nanotechnology and Innovation for giving me this opportunity of study. I acknowledge my funding Mintek as well as Desmond Goddard for the financial support they provided me through my MSc.

Abstract

The work focuses on the development of biosensors and their use for the detection of prostate specific antigen (PSA). Four cobalt phthalocyanines (CoPcs) complexes: (**1**) cobalt tetra pyridyloxy phthalocyanine, (**2**) cobalt tetra acetamidophenoxy phthalocyanine, (**3**) cobalt tris(acetamidophenoxy) mono benzoic acid phthalocyanine, and (**4**) cobalt tris(acetamidophenoxy) mono propionic acid phthalocyanine, an exfoliated graphite (EG), and aptamer are used to make probes for PSA detection. Each complex is π-π stacked onto the EG to form EG-CoPc(π-π) hybrid which was used to modify a glassy carbon electrode (GCE). EG and CoPc were also used to modify the GCE sequential (seq) with CoPc on top to give GCE-EG-CoPc(seq). For the detection PSA, PSA specific aptamer was either sequential added or covalently linked to complexes **3** and **4** on the modified electrodes and was only sequentially added onto complexes **1** and **2** modified electrodes. Electrochemical impedance spectroscopy (EIS) and differential pulse voltammetry (DPV) were the techniques used for the detection of PSA. The electrodes were found to be selective in bovine serum albumin, glucose and cysteine and stable when 50 DPV scans were run. Electrodes gave good % recovery when human serum was spiked with different PSA concentrations.

Table of contents

List of abbreviations

Ads	Adsorbed
Anal. Calcd	Analytical Calculated
BSA	Bovine serum albumin
BET	Brunauer–Emmett–Teller
Cov	Covalent
CV	Cyclic voltammetry
DBU	1,8-Diazabicyclo [5.4.0] undec-7-ene
DCC	Dicyclohexylcarbodiimide
DPV	Differential pulse voltammetry
DMF	Dimethylformamide
EIS	Electrochemical impedance spectroscopy
EDS	Energy-dispersive X-ray spectroscopy
EG	Exfoliated graphite
FT-IR	Fourier transform-infrared
GCE	Glassy carbon electrode
AuNPs	Gold nanoparticles
GIC	Graphite intercalation compound
gCNQDs	Graphitic carbon nitride quantum dots
GQDs-AuNRs	Graphene quantum dots gold nanorods
IR	Infrared red
LoD	Limit of detection
MALDI-TOF	Matrix assisted laser-desorption/ionization-time of flight

NGF	Natural graphite flake
NHS	N-hydroxysuccinimide
NGQDs	Nitrogen doped graphene quantum dot
Pc(s)	Phthalocyanine(s)
Pt	Platinum wire
PSA	Prostate specific antigen
SEM	Scanning electron microscope
SPE	Screen printed electrode
Seq	Sequential
THF	Tetrahydrofuran
TGA	Thermogravimetric Analysis
UV-Vis	Ultraviolet-visible
XRD	X-ray diffraction

List of symbols

I_{PSA}	Background corrected current of the PSA
I_{mixure}	Background corrected current of the PSA and interference
R_{ct}	Charge transfer resistance
[PSA]	Concentration of PSA
g	Grams
λ_{max}	Lamda max\wavelength
log ε	Logarithm of molar absorptivity
mmol	Millimoles
β	Non-Pheripheral position
∆Ep	Peak potential separation
%	Percentage
α	Pheripheral position
π	Pi
K_{AMP}	Selective coefficient
Ag|AgCl	Silver|Silver Chloride

Preface

Prostate cancer is one of the frequent cancers in men who are above 50 years old. Early detection of prostate cancer plays a significant role in reducing mortality rates and improving the patients' prognosis. The methods such as mammograms, ultrasound etc., which are currently used, are expensive and require trained personnel. In this research electrochemical biosensors are employed. The electrochemical biosensors are cheap, robust, easy to miniaturize, have excellent detection limits using small analyte volumes. In this work the use of phthalocyanines (Pcs) of different symmetries are employed. Adding the nanomaterials (exfoliated graphite (EG)) to the Pcs improved the functioning of the biosensor. The Pc and EG are known as electrocatalysts and they were successfully applied in this work to make biosensors. The use of MPc in the presence of EG as electrocatalysts is presented in this work for the first time.

Chapter 1: Introduction

In this Chapter MPcs, EG and EG-MPc conjugates with aptamers are introduced for the use as biosensors in detecting the PSA.

1.1. The overview of metallophthalocyanines (MPcs)

1.1.1. The General Structure and Application

Phthalocyanines (Pcs) are macrocyclic compounds made up of four isoindole units linked by a nitrogen atom (**Scheme 1.1**) [1, 2]. Pcs are 18 π electron aromatic and planar macrocycles which have found applications in for example: molecular electronics [3], metal sensors [4-6], liquid crystals [7], photovoltaic cells [8], Langmuir-Blodgett films [9], non-linear optics [10] and photodynamic therapy [11] to name a few. The cavity of phthalocyanines can hold over 70 different metals and metalloids [12]. The phthalocyanines can be substituted at the peripheral (α) and non-peripheral (β) positions with different groups for different applications (**Scheme 1.1**). Metallophthalocyanines (MPcs) containing transition metals such as Mn, Co, Ni, Fe and Cu have been successfully employed as electrocatalysts in electrochemical sensing and the electrocatalytic activity of MPcs has been reported to be of the following order (depending on the central metal): $Fe^{2+} > Co^{2+} > Mn^{2+} > Ni^{2+} \approx Cu^{2+}$, with Co^{2+} and Fe^{2+} being the most extensively studied [13], hence CoPc derivatives are employed in this work. Electrocatalysts takes part in electrochemical reactions to increase the reaction rate at the electrode surface [14]. This work focuses on the electrocatalytic behaviour of the cobalt Pc for prostate specific antigen (PSA) detection.

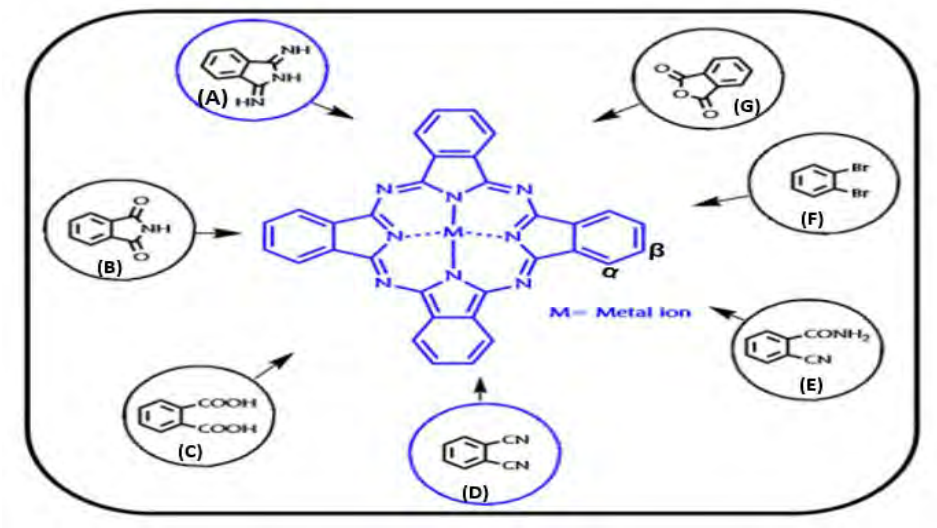

Scheme 1.1: The typical structure of phthalocyanine and different starting materials: A = 1,3-isoindolinediimine, B = 1,3-isoindolinedione, C = phthalic acid, D = phthalonitrile, E = 2-cyanobenzamide, F = dibromobenzene, G = 3-oxydanylidenephthalide.

1.1.2. UV-Vis Spectra

Pcs show absorption in the red/near-infrared and ultraviolet regions called Q and B bands respectively (**Fig. 1.1**) [15]. In MPcs, the single intense Q band is associated with D_{4h} symmetry due to π-π* transitions from the a_{1u} of highest occupied molecular orbital (HOMO) to e_g* of lowest unoccupied molecular orbital (LUMO). The broad B-band is due to transitions between a_{2u} and b_{1u} (HOMO) to e_g* orbitals (LUMO) as shown in **Fig 1.1** [16].

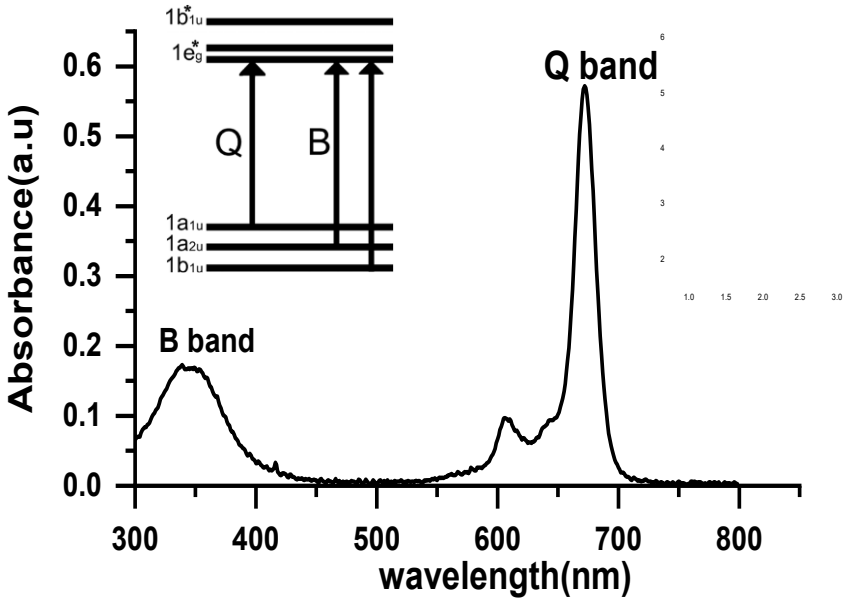

Fig. 1.1: UV-Vis spectroscopical characteristics of a Zn standard phthalocyanine (insert: Electronic energy level transitions in metal phthalocyanine complexes).

1.1.3. Synthesis

The general synthesis of metallophthalocyanines (MPcs) involves the utilization of precursors such as phthalonitrile, phthalimide, phthalic anhydride, phthalic acid, phthalimide, o-cyonobenzomide or 1,3-diiminooisoindoline (**Scheme 1.1**). The precursors are added with a metal salt (e.g cobalt(II) chloride) and catalyst which can be a non-nucleophilic base (1,8-diazabicyclo[5.4.0]undec-7-ene (DBU) or 1,5-diazabicyclo[4.3.0]non-5-ene (DBN)), refluxed at high boiling solvents; such as dimethylformamide (DMF), dimethylethanolamine (DMAE). Phthalonitrile is the precursor that is mostly used to synthesize the Pc in the laboratory. There are two types of MPcs -symmetrical and asymmetrical. The symmetrical MPcs are synthesised from one phthalonitrile, whereas asymmetrical involves two different phthalonitriles [17].

1.1.3.1. Symmetrically substituted MPc

The synthesis of a symmetrically substituted phthalocyanine is done by cyclotetramerisation of the phthalonitrile in the presence of a catalyst and a metal salt at relatively high temperatures [18]. The condensation of a single phthalonitrile (**Scheme 1.2**) results in a statistical mixture of Pc structural isomer units which are D_2h, C_4h, C_2v and C_s symmetry [19]. The yield of the desired product depends on the substituent and the amount of phthalonitrile relative to the metal salt [17].

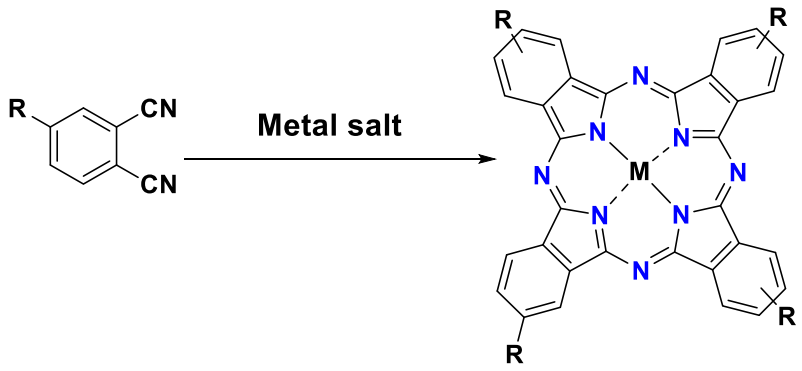

Scheme 1.2: Symmetric synthesis of the phthalocyanine.

1.1.3.2. Asymmetrically substituted MPcs

Asymmetrically substituted phthalocyanine synthesis involves, the statistical condensation reaction of two differently substituted phthalonitriles (**Scheme 1.3**) [20]. Combination of phthalonitriles is in a ratio of 3:1, 9:1, or higher depending on the reactivity of the phthalonitriles [20]. This type of synthesis also results in the formation of isomers in which the desired product from these isomers is obtained by a column chromatography. The yields following column chromatography are low.

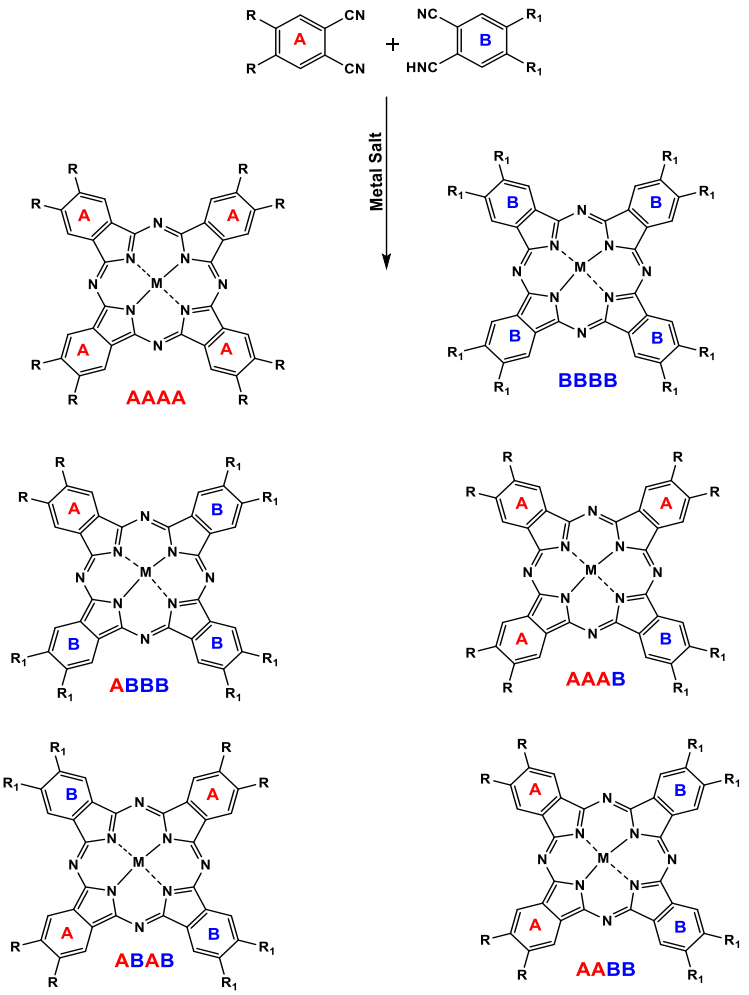

Scheme 1.3: Asymmetric synthesis of the phthalocyanine and its possible isomers.

1.1.4. MPcs used in this work

Four different phthalocyanines were synthesized in this work which are; (**1**) cobalt (II)tetra(pyridyloxy)phthalocyanine,(**2**)cobalt(II)(tetraacetamidophenoxy)phthalocyani ne, (**3**) cobalt(II)4-(carboxyphenyl)tris(acetamidophenoxy)phthalocyanine, and (**4**) cobalt(II)4-(carboxypropanyl)tris(acetamidophenoxy)phthalocyanine (**Table 1.1**). Complexes **1** and **2** are known [21, 22], while complexes **3** and **4** are new. Complexes **1** and **2** are symmetrically substituted MPs, while complexes; **3** and **4** are

asymmetrically substituted. These complexes were studied for the effect of symmetry in detecting the analyte of interest which is the prostate specific antigen (PSA). Cobalt is used as a central metal due to the known electrocatalytic activity of CoPc [13]. The acetomidophenoxy was chosen for complexes **2**, **3** and **4** since it has an internal push-pull effect, improving electrocatalytic activity [23]. The CoPcs are used in combination with exfoliated graphite (EG) and an aptamer for the detection of PSA.

Table 1.1: Structures of MPcs employed in this work

COMPLEXES	COMPLEXES
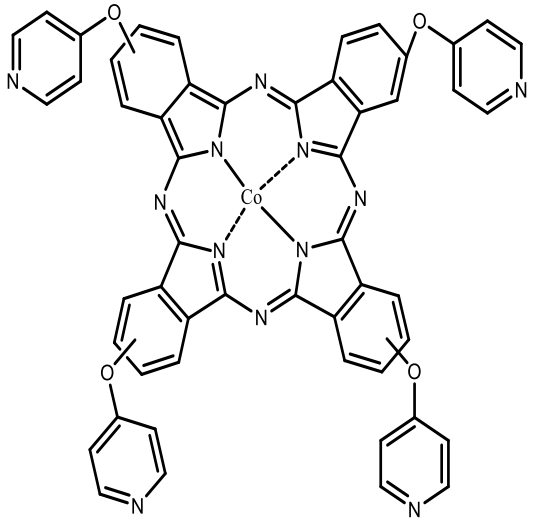 **known [21] (Complex 1)** **cobalt (II)tetra(pyridyloxy)Pc1**	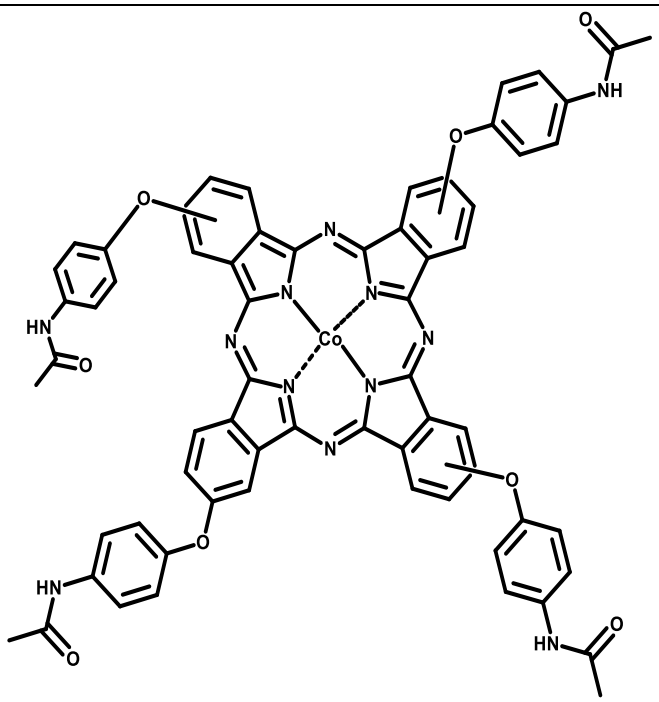 **known [22] (Complex 2)** **cobalt(II)(tetraacetamidophenoxy)Pc2**

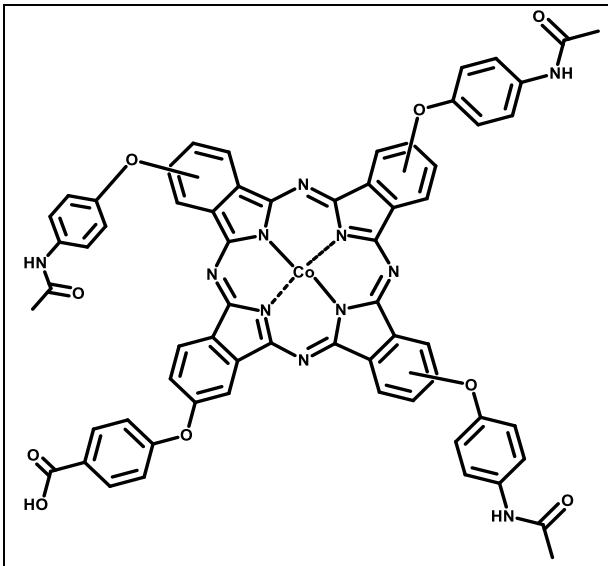 **New** **(Complex 3)** **cobalt(II)4-(carboxyphenyl)tris(acetamidophenoxy)Pc3**	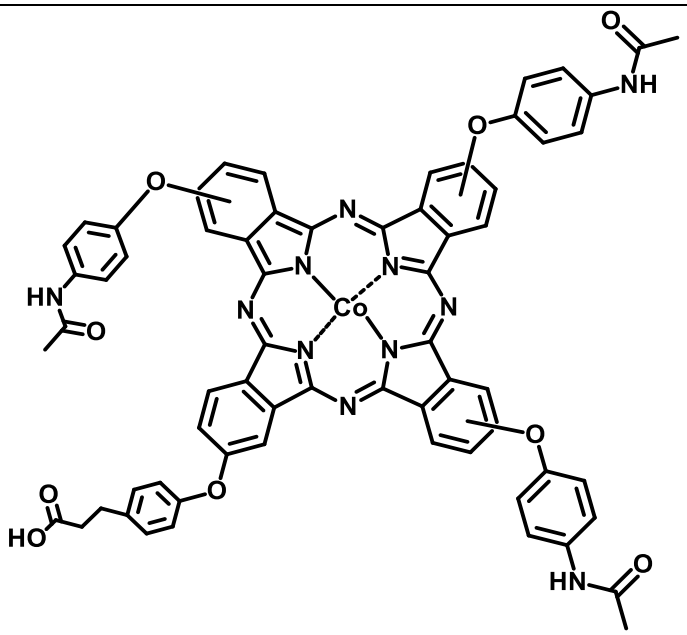 **New** **(Complex 4)** **cobalt(II)4-(carboxypropanyl)tris(acetamidophenoxy)Pc4**

1.2. Exfoliated graphite

The exfoliated graphite (EG) refers to the graphite that has a degree of separation of substantial portions of the adjacent carbon layers [24]. This separation may or may not occur in all carbon layers [24]. To separate the adjacent carbon layers; chemical, and thermal methods can be used (**Fig. 1.2**). Separating the entire plane may result in different pieces of EG which have a small number of carbon layers [24]. Along the c-axis of the structure, van der waals forces maintain the carbon layers at about 3.35 A˚ apart [24, 25]. This feature allows the EG to be flaky [26]. In preparation of EG, different graphite intercalation compounds (GIC) may form. GIC may be divided into two groups: covalent and ionic [27]. The most studied graphitic material is ionic GIC [28]**.** EG can be used as an electrocatalyst and can enhance the electrocatalytic

activity of other materials [29-31]. MPcs are also very well-known electrocatalysts [32-34]. There is only one report on the use of cobalt phthalocyanine together with EG for development of composite electrode [35]. This is the first report of Pc used for electrocatalysis in the presence of EG. The combination of Pc with EG may improve electrocatalytic activity by synergy.

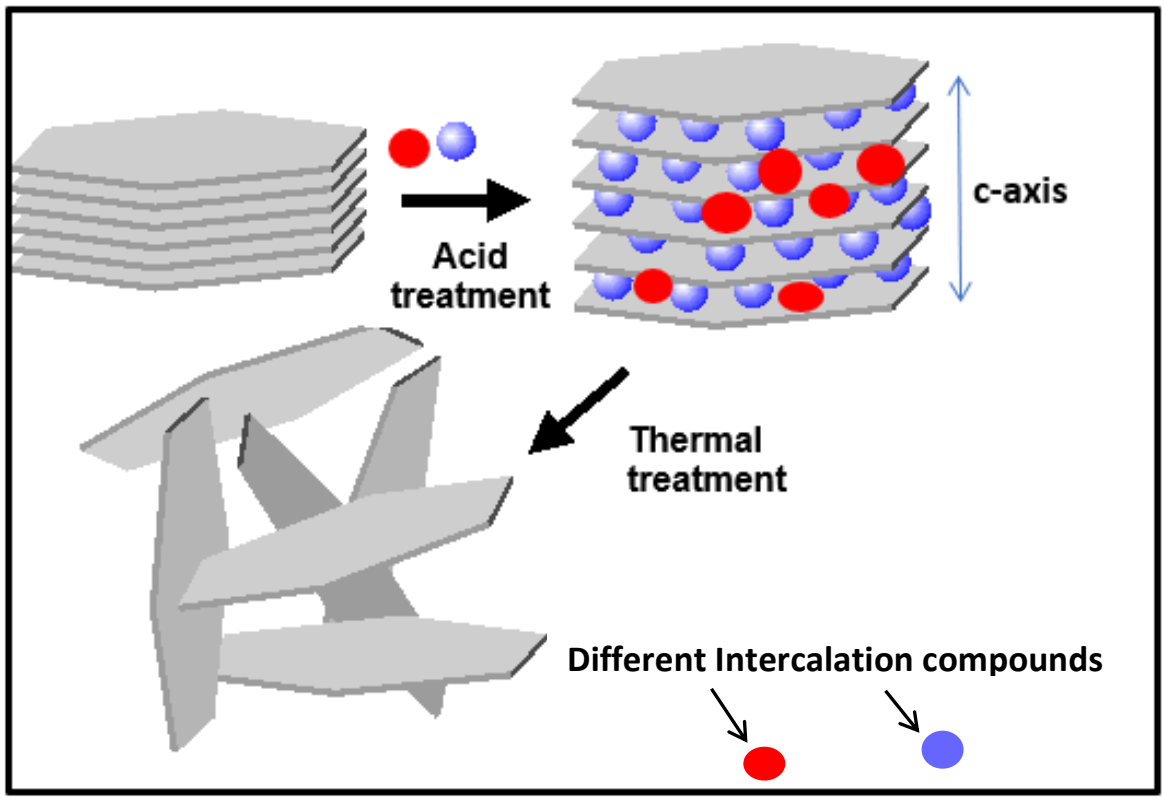

Fig. 1.2: The layered structure of EG, which underwent exfoliation through chemical and thermal treatments.

1.2.1. Exfoliated graphite synthesis

The synthesis of EG involves the chemical and thermal treatment of graphitic material such as natural graphite flakes (**Fig. 1.2**). Graphite reacts with a wide range of intercalates to form intercalation compounds which are referred to as acid salts of graphite. The most widely studied graphite intercalated acids are sulphuric acid, nitric

acid, perchloric acid, selenic acid [36]. There are three techniques that can be used to prepare GIC, chemical oxidation, gas phase intercalation and electrochemical intercalation [37]. Chemical oxidation [38] and electrochemical intercalation [39] are the commonly used methods, however chemical oxidation is preferred the most because it is more convenient, cheap and results in highly stable EG [40]. The chemical oxidation method involves the use of oxidant and intercalating agent such as nitric acid and sulphuric acid [41, 42], as shown by **Fig. 1.2** in which two intercalates are used.

1.2.2. Exfoliated graphite composite with different materials

Different materials are added to or with EG to form different composites. There is only one report on the use of cobalt phthalocyanine together with EG for development of composite electrode as previously mentioned [35], however the EG electrodes have been synthesized and employed with different materials for different applications [43-58] (**Table. 1.2**). EG and MPc have π-electrons and can be π-π stacked and added to a glassy carbon electrode (GCE) by a drop and dry method for electrochemical applications as is the case in this work.

Table 1.2: Known examples of exfoliated graphite with different materials to make electrodes for various applications.

Conjugates	**Application**	**references**
EG-CoPc	Electrocatalytic oxidation	[35]
EG-AuNPs	Molecular sensing	[43-45]
EG -BiNPs	Molecular sensing	[46]
EG -CoNPs-rGO	Molecular sensing	[47]
EG -CoNPs	Molecular sensing	[48]
EG -PPI	Molecular sensing	[49]
EG-$BiVO_4$	Photoelectrode gradation	[50]
EG-$BiVO_4$/ZnO	Photoelectrode gradation	[51]
EG-WO_3	Photoelectrode gradation	[52]
EG-TiO_2	Photoelectrode gradation	[53]
EG-ZnO	Photoelectrode gradation	[54]

EG-CeO_2	Photoelectrode gradation	[55]
EG-MoO_3	Photoelectrode gradation	[56]
EG-Ag/ZrO_2	Photoelectrode gradation	[57]
EG-Ag/Ag_3PO_4	Photoelectrode gradation	[58]

Abbreviations: NPs=Nanoparticles, rGO=reduced graphene oxide, PPI=Poly Propyl imine

1.3. Biosensors and Sensing

A biosensor is an analytical device in which a biological compound, signal transducer and an amplifier are coupled together. There are various types of biosensors, which are- enzyme-based, tissue-based, immunosensors, DNA-based, thermal, piezoelectric, and magnetic biosensors; to mention a few [59]. **Fig 1.3** shows components of a biosensor, characterized by a biorecognition element which is fixed on the surface of the electrode either by physical or chemical method. The bio-recognition element then selectively identifies the target molecule on the electrode surface. The contact of the target molecule with the bio-recognition element results in a reaction that is transformed into electrochemical signal that is latter displayed on the screen. Electrochemical signals include, current, voltage, and resistance that can be measured and analysed quantitative or qualitatively [60]. The chosen biosensor in this work is the DNA biosensor. The Pc/EG with an aptamer were employed for the recognition of PSA, following modification of GCE.

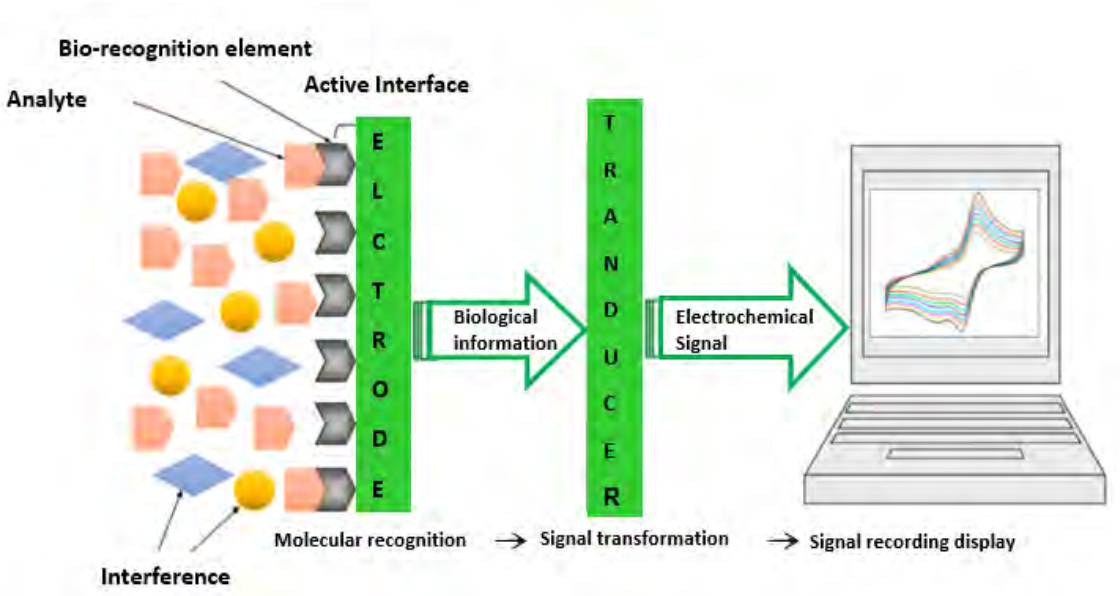

Fig.1.3: Showing different parts of the biosensor [60].

1.4. Electrode modification

The drop and dry method was chosen in this work because it is simple and less time consuming. The technique involves a sampling of the compound and dropping it onto GCE, followed by drying in inert environment to achieve immobilization of the compound. In **Fig.1.4**, the compound of choice is the MPc however, EG is also drop and dried the same way**.** In the presence of a Pc/EG on GCE, a DNA can also be dropped onto the GCE**. Scheme 1.4** shows the immobilization of MPc in the presence nanomaterials such as graphitic carbon nitride quantum dots (gCNQDs). The aptamer is adsorbed to the MPcs in **Scheme 1.4**.

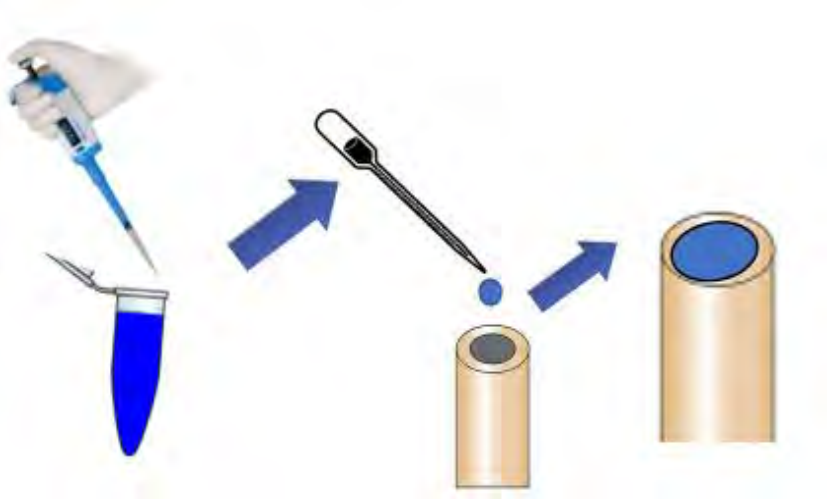

Fig.1.4: General procedure of drop and dry method on bare GCE. (**1**). Sampling of MPc, (**2**) dropping of MPc onto GCE, (**3**) drying in an inert environment.

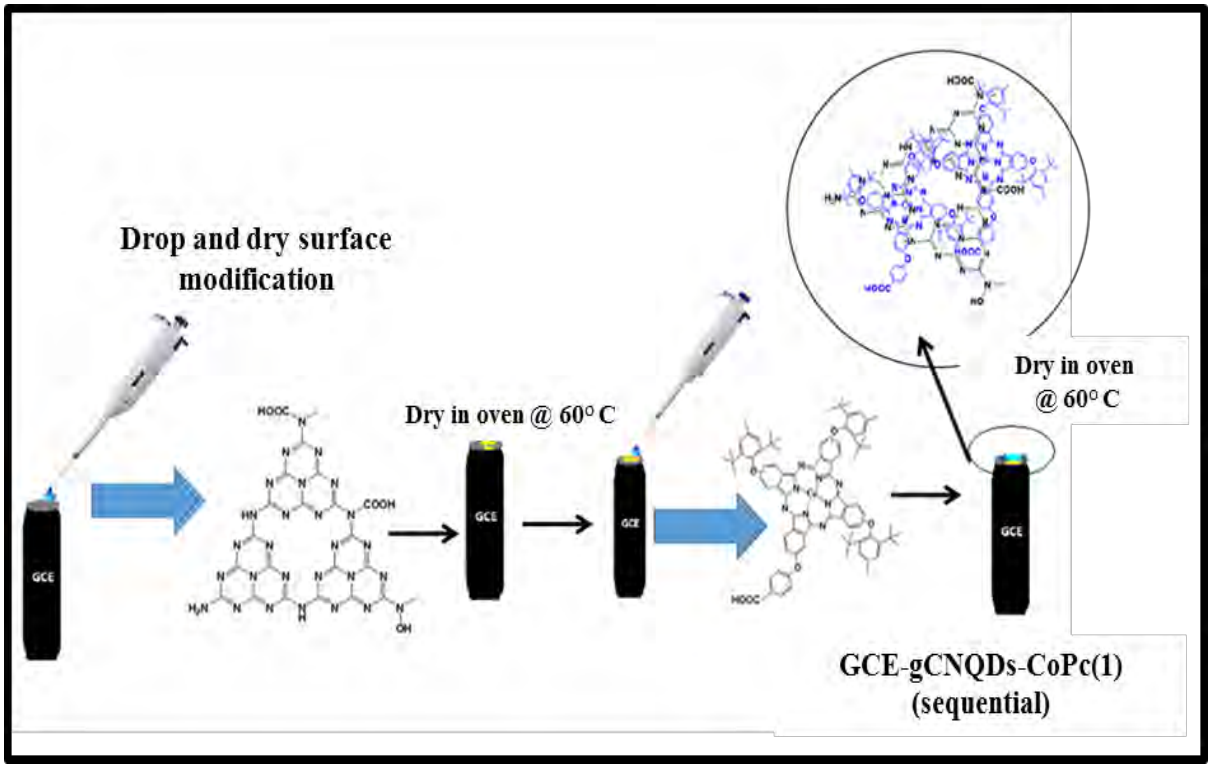

Scheme 1.4. Represent the GCE to GCE-CoPc/gCNQDs (sequential). gCNQDs= graphitic carbon nitride quantum dots [61].

1.5. Analyte employed in this work and application

Prostate specific antigen (PSA) is a serine protease or a single chain of glycoprotein with a molecular weight of 32-33 kDa [62, 63]. PSA is released into the blood from the serum, seminal plasma, benign hyperplastic and prostatic fluids, and this helps in the initial diagnosis and monitoring of the response to treatment [64, 65]. The level of PSA is then monitored; PSA level below 4 ng/ml is regarded as normal, between 4 and 10 ng/ml is a grey zone and above 10 ng/ml is considered as positive and the indication of the prostate cancer [62]. Prostate cancer symptoms present themselves at a later stage and so a PSA blood test is used since it found to be more sensitive [62]. In this work the PSA is used with an aptamer. An aptamer is oligonucleotide or single stranded DNA or RNA that binds specifically to the antigen which is PSA in this work as shown as an example in **Fig 1.5 (a)** [62]. Several immunosensors have been fabricated for the detection of PSA using antibodies as biorecognition elements (**Fig 1.5 (b)**) [66-68], however aptamers have high sensitivity, selectivity and stability compared to antibodies [69, 70], hence a PSA specific aptamer is employed. The PSA specifically binds to the PSA specific aptamer that is immobilized at the electrode surface. Detecting PSA using an antibody is known to decrease the reaction activity [71]. One of the most important advantages of using an aptamer than an antibody, is that there are no limitations to their targets [72]. **Table 1.3** shows CoPc and different nanoparticles used for the detection of PSA in the presence of an aptamer and antibody [73-76]. This work presents the first time, CoPc is used in the presence of EG.

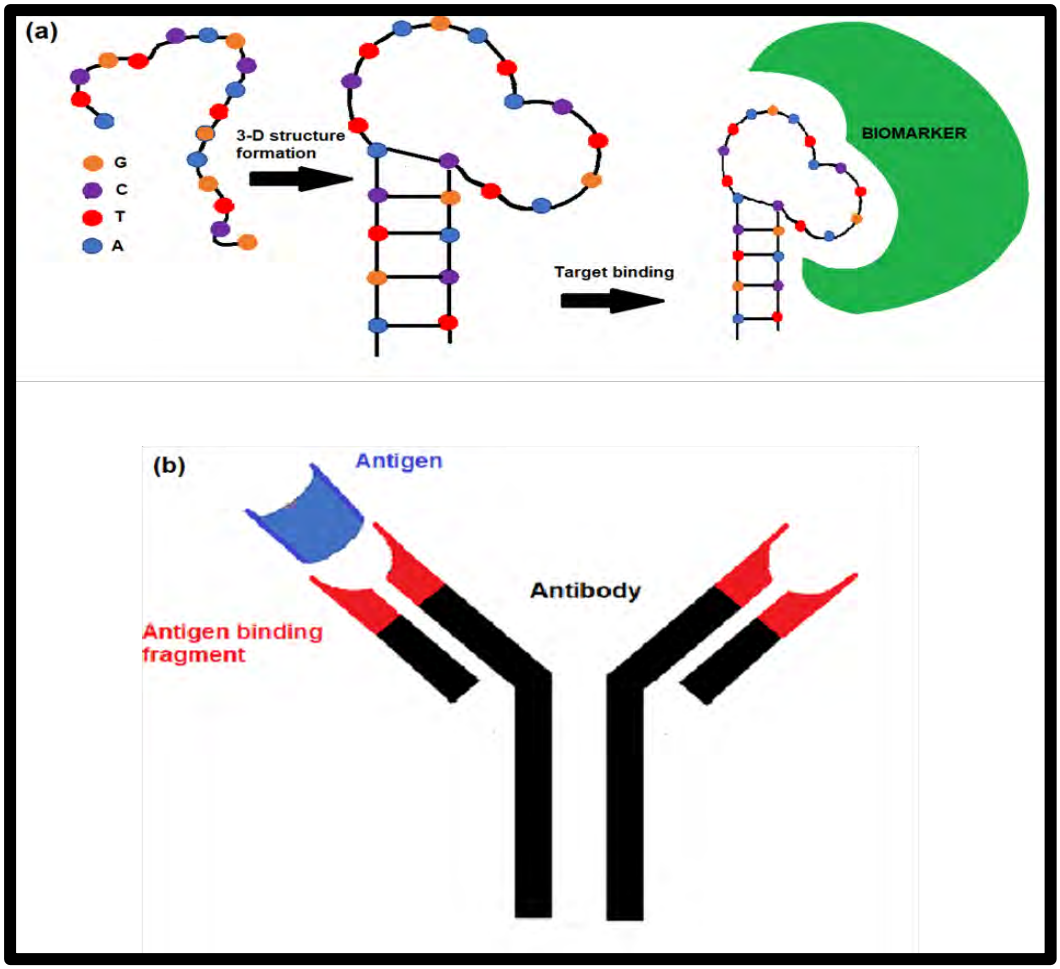

Figure 1.5: Schematic representation of binding **(a)** an aptamer and (b) an antibody to a biomarker.

Table 1.3: Electrochemical detection of a PSA using Pcs, antibodies, and aptamers with different nanomaterials.

Electrode	**Recognition element**	**references**
GCE-gCNGQDs-CoPc and GCE-NGQDs-CoPc GCE-gCNGQDs-CoPc and GCE-GQDs-CoPc **CoPc**= 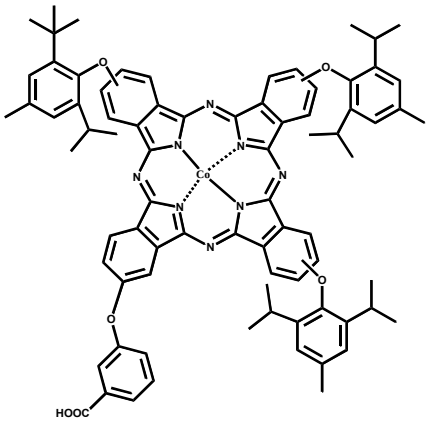	Aptamer	[73, 74]
GCE-AuNPs-CoPc and GCE-gCNGQDs-CoPc 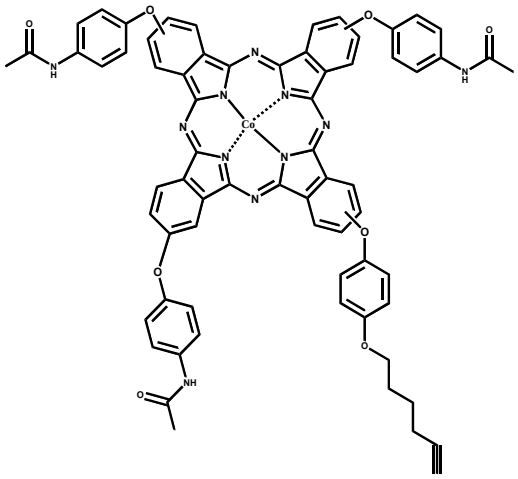 **CoPc**=	Aptamer	[74, 75]

GCE- (G–CdS) -CoPc 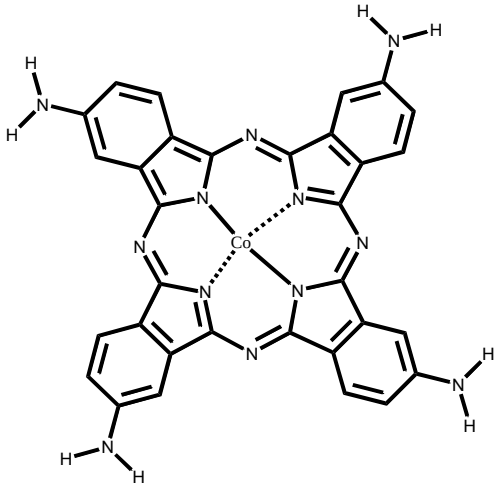 **CoPc**=	Antibody	[76]

Abbreviations: gCNGQDs= graphitic carbon nitride quantum dots, AuNPs= gold nanoparticles, G-Cds= graphene–CdS, GQDs= graphene quantum dots, NGQDs= nitrogen doped graphene quantum dots.

1.6. The summary of aims and objectives of this work

Aim: To design a highly sensitive and selective electrochemical biosensor for PSA.

Objective:

1. Synthesis and characterization of graphitic nanomaterials

2. Synthesis and characterization of metal phthalocyanines (symmetrical and asymmetrical)

3. π-π stacking of metal phthalocyanines and graphitic nanomaterial for electrode modification

4. Characterize the synthesized phthalocyanine, graphitic nanomaterial, and the conjugate using UV-Vis. Note: Other methods were also used.

5. Electrode modification with the resulting phthalocyanines/graphitic nanoconjugates and the phthalocyanine/ PSA-aptamer, graphitic nanomaterial/ PSA-aptamer, and phthalocyanines/graphitic nano-conjugate-PSA-aptamer. Aptamer to be used: ssDNA): 5′-NH_2-$(CH_2)_6$-TTT TTA ATT AAA GCT CGC CAT CAA ATA GCT TT-3′ (235 nmol, >90% purity).

6. Use of electrochemical measurements to determine the activity of the biosensor.

7. To compare the effect of the biosensor when an aptamer is adsorbed and covalently linked to asymmetric phthalocyanines to study the impact of symmetry of MPc on a biosensor.

Chapter 2: Materials, Equipment, and Experimental

This chapter presents materials and equipment used in this work. The synthesis of the phthalocyanines, exfoliated graphite, and their conjugates, as well as electrode modification methods employed.

2. Materials and Experimental

2.1. Materials

Iron ferricyanide, iron ferrocyanide, natural graphite flakes (NGF), 1,8-diazabicyclo[5.4.0]undec-7-ene , potassium chloride, cobalt chloride ($CoCl_2$), cysteine, glucose, N-hydroxysuccinimide (NHS), 1,3-dicyclohexylcarbodiimide (DCC), human serum (H6914), bovine serum albumin (BSA), and prostate specific antigen (PSA), were obtained from Sigma–Aldrich. Tetrahydrofuran (THF) and dimethylformamide (DMF) were obtained from Merck. The amine-functionalized PSA specific aptamer was synthesized by (and purchased from) Integrated DNA Technologies (IDT) and purified using high-performance liquid chromatography, and its sequence is as follows: 5′ -NH_2-$(CH_2)_6$-TTT TTA ATT AAA GCT CGC CAT CAA ATA GCT TT-3′ (235 nmol, >90% purity). Phosphate buffer saline (PBS, pH 7.4) was prepared by weighing appropriate amounts of Na_2HPO_4, KH_2PO_4, KCl, and NaCl in ultra-pure water from ELGA, Veolia PURELAB, flex system (Marlow, UK). *N*-(4-(3,4-dicyanophenoxy) phenyl) acetamide phthalonitrile (**A**) [77], 4-(3,4-dicyanophenoxy) benzoic acid (phthalonitrile **B**) [78], 3-(4-(3,4-dicyanophenoxy) phenyl) propanoic acid (phthalonitrile **C**) [79] (**Scheme 3.1**), and exfoliated graphite [80] were synthesized as reported in the literature. Complexes **1** and **2** were synthesized as reported in the literature [21, 22].

2.2. Equipment

Ultraviolet-visible (UV–Vis) absorption spectra were recorded using a Shimadzu UV-2250 spectrophotometer. X-ray diffraction (XRD) analysis was performed on a Bruker D8 Discover diffractometer, equipped with a Lynx Eye detector, under Cu Kα radiation (λ= 1.5405 Å). Scanning electron microscopy (SEM) images were obtained using a

TESCAN Vega TS 5136 LM electron microscope. A three-electrode electrochemical cell made up of a glassy carbon electrode (GCE, 3 mm diameter) - working electrode, platinum wire (Pt) counter electrode, and silver|silver chloride (Ag|AgCl in 3.0 M KCl) as reference electrode was employed. Electrochemical impedance spectroscopy (EIS), differential pulse voltammetry (DPV) and cyclic voltammetry (CV) studies were performed using an Autolab Potentiostat PGSTAT30 equipped with Nova software version 2.1. EIS studies were conducted between 0.1 Hz and 10 Hz, using a 5 mV rms sinusoidal modulation. Elemental compositions of the CoPc, EG, and CoPc-EG were qualitatively determined using energy-dispersive X-ray spectroscopy (EDS). The thermal stability of the materials was studied using a Perkin-Elmer TGA 7 analyzer. Heating rate was suitably maintained at 10 °C min^{-1} under nitrogen gas from 50 °C up to 1000 °C. A Bruker Vertex 70-Ram II Raman spectrometer (equipped with a 1064 nm Nd: YAG laser and liquid nitrogen-cooled germanium detector) was used to collect Raman data. The nitrogen adsorption/desorption isotherms were carried out at 77 °K using a Micrometrics ASAP 2020 Surface area and Porosity analyzer. Before each measurement, degassing was carried out at 90 °C for two days. The Brunauer–Emmett–Teller (BET) method was employed to determine surface area and porosity. Micropore average pore diameter and BET micropore surface areas were obtained directly from the t-plot tabular report. Mass spectral data were obtained on a Bruker Auto FLEX III Smart-beam TOF/TOF mass spectrometer, using a-cyano-4-hydrocinnamic acid as the matrix in the positive ion mode. The desired CoPc was purified to remove impurities using column chromatography with silica gel (Merck grade 60).

2.3. Synthesis

2.3.1. CoPc derivatives

2.3.1.1. Cobalt tris(acetamidophenoxy)mono benzoic acid Pc (3), Scheme 3.1

N-(4-(3,4-dicyanophenoxy)phenyl)acetamide (**A**) (0.41 g, 1.5 mmol), 4-(3,4-dicyanophenoxy)benzoic acid (**B**) **(**0.076 g, 0.29 mmol), and $CoCl_2$ (0.094 g, 0.72 mmol) were added to dry DMF (10 mL) in the presence of catalytic amounts of DBU (0.5 mL). The mixture was refluxed for 24 h in an argon atmosphere. Following the completion of the reaction, the product was allowed to cool to room temperature, after which the crude sample was precipitated using methanol and water and then dried in an oven at 60 °C. The desired compound was obtained as the fourth fraction, where silica gel (SiO_{60}) served as the stationary phase and a solvent mixture of DMF and acetic acid served as the mobile phase. (v/v 9:1). Yield: 60.4 mg, 15.9 % (w/w); UV/Vis (DMF): λ_{max}/nm (log Ɛ): 668 (4.14), 609 (3.72), 325 (4.04). IR [(KBr), ν_{max}/cm^{-1}]: 746 (aromatic C-H_{str}), 1089 (primary alcohol C-O-C_{str}), 1225 (alkyl ether O-C_{str}), 1401 (carboxylic acid OH_{bend}), 1503 (aliphatic C-H_{str}), 1660 (secondary amide C=O_{str}), 3053 (alkene C-H_{str}). Anal. calc. for $C_{63}H_{49}CoN_{11}O_9 \bullet 4H_2O$: C, 61.7; N, 12.6. Found: C, 60.4; N, 12.3. MS (MALDI-TOF) (m/z): calc.: 1154.24 amu; found: 1155.82 amu $[M+H]^+$ (**Fig. A1**) (Appendix).

2.3.1.2. Cobalt tris(acetamidophenoxy)mono propionic acid Pc(4), Scheme 3.1

The synthesis of complex **4** was the same as for complex **3,** except that 4-(3,4-dicyanophenoxy) phenylpropanoic acid (**C**) (0.10 g, 0.36 mmol) was used instead of 4-(3,4-dicyanophenoxybenzoic acid (**B**). The amounts of all the other reagents were

the same, as were the reaction conditions and purification methods, except for complex **4**. Hot methanol was used to purify the final product. Yield: 49.7 mg, 13.0 % (w/w); UV/Vis (DMF): λ_{max}/nm (log Ɛ): 667 (4.42), 610 (4.08), 324 (4.41). IR [(KBr), ν_{max}/cm^{-1}]: 746 (aromatic C-H_{str}), 1091 (primary alcohol C-O_{str}), 1229 (alkyl ether O-C_{str}), 1403 (carboxylic acid OH_{bend}), 1503 (alkane C-H_{bend}), 1656 (secondary amide C=O_{str}), 2936 (aliphatic C-H_{str}), 3051 (alkene C-H_{str}). Anal. calc. for $C_{65}H_{45}CoN_{11}O_9 \bullet 5H_2O$: C, 61.3; N, 12.1. Found: C, 61.3; N; 12.2. MS (MALDI-TOF) (m/z): calc.: 1182.27 amu; found: 1182.76 amu $[M]^+$ (**Fig. A2**) (Appendix).

2.3.2. Synthesis of exfoliated graphite (EG), Scheme 3.2

Natural graphite flakes (NGF) were immersed in a mixture of concentrated H_2SO_4/HNO_3 (3:1 (v/v)) for 24 h at ambient temperature. The graphite intercalated compound (GIC) was obtained and was washed with a copious amount of distilled water until a pH of 7 was reached. The neutral GIC material was air-dried. Exfoliation was performed by exposing the GIC to a thermal shock of 900 °C in a preheated furnace for a minute, resulting in a material with very low density called exfoliated graphite.

2.3.3. Synthesis of π-π stacked EG-CoPc hybrid, Scheme 3.3

The π-π stacking of CoPcs ((**1**), (**2**), (**3**), and (**4**)) onto EG was done by adding each CoPc complex (10 mg) separately to EG (20 mg) in 5 mL DMF, followed by stirring for 72 h at room temperature to give EG-(**1**)(π-π), EG-(**2**)(π-π), EG-(**3**)(π-π), and EG-(**4**)(π-π).

2.4. Electrode modification

The glassy carbon electrode (GCE) was used in this work as the working electrode. GCE was thoroughly polished to a silver mirror on a Buehler-Felt pad in a slurry made from alumina nanopowder and then washed with Millipore water. Modifications to the electrode were conducted as follows: 1 mg of each material of CoPc (**1-4**), EG, and EG-CoPc(π-π) were dissolved in 1 mL of DMF separately and sonicated. A 5 µL of CoPc, EG, and EG-CoPc(π-π) was dropped on GCE separately and dried in an oven at 60 °C. The GCE was also modified by the sequential(seq) addition of EG followed by CoPc onto the GCE (without allowing time for π-π interaction). We have shown that the best catalytic activity was obtained when MPcs are placed on top of nanomaterials [81]; hence, in this work, for the sequentially modified electrodes, EG is placed first on the electrode, followed by the CoPc derivative to give GCE-EG-CoPc. The electrodes are: GCE-(**1**), GCE-(**2**), GCE-(**3**), GCE-(**4**), GCE-EG, GCE-EG-(**1**)(seq)**,** GCE-EG-(**2**)(seq), GCE-EG-(**3**)(seq), GCE-EG-(**4**)(seq), GCE-EG-(**1**)(π-π), GCE-EG-(**2**)(π-π), GCE-EG-(**3**)(π-π), and GCE-EG-(**4**)(π-π). Please note: for the electrodes containing both EG and CoPc, sequential(seq) was used for electrodes modified with both EG and MPc and without allowing time for π-π bonds, and π-π was used where there was time allowed for the formation of the bonds. An aptamer was introduced into these electrodes and before use the aptamer underwent the folding process. This was done by heating each solution of the different concentrations of an aptamer (0.25–2.0 µM) in phosphate buffer saline (PBS) at 89 °C for 5 min and cooled at room temperature for 15 min [82]. The folding process is known to result in the colloidal stabilization of the aptamer. Aptamer concentrations of 0.25–2.0 µM were employed to determine the optimum aptamer concentration as follows, an aptamer was adsorbed onto GCE-(**1**) (as an example), and cyclic voltammograms were recorded in $[Fe(CN)_6]^{3-/4-}$ (1 mM in

0.1M KCl). The resulting currents were plotted against aptamer concentration, **Fig. 2.1**. The current increased at 0.75 µM of an aptamer, then decreased and rose again at 1.5 µM and 2 µM. The first maximum of 0.75 µM was employed throughout all studies to minimize costs. The aptamer (5 µL of 0.75 µM) was adsorbed (represented as ads) on the surface of the GCE electrode and allowed to dry to give the electrodes: GCE-aptamer, GCE-(**1**)-aptamer, GCE-(**2)-**aptamer, GCE-(**3**)-aptamer(ads), GCE-(**4**)-aptamer (ads) GCE-EG-aptamer, GCE-EG-(**1**)(seq)-aptamer, GCE-EG-(**2**)(seq)-aptamer, GCE-EG-(**3**)(seq)-aptamer(ads), GCE-EG-(**1**)(π-π)-aptamer, GCE-EG-(**2**)(π-π)-aptamer, GCE-EG-(**3**)(π-π)-aptamer(ads), GCE-EG-(**4**)(seq)-aptamer(ads) (**Scheme 4.1**) (using complex **3** as an example).

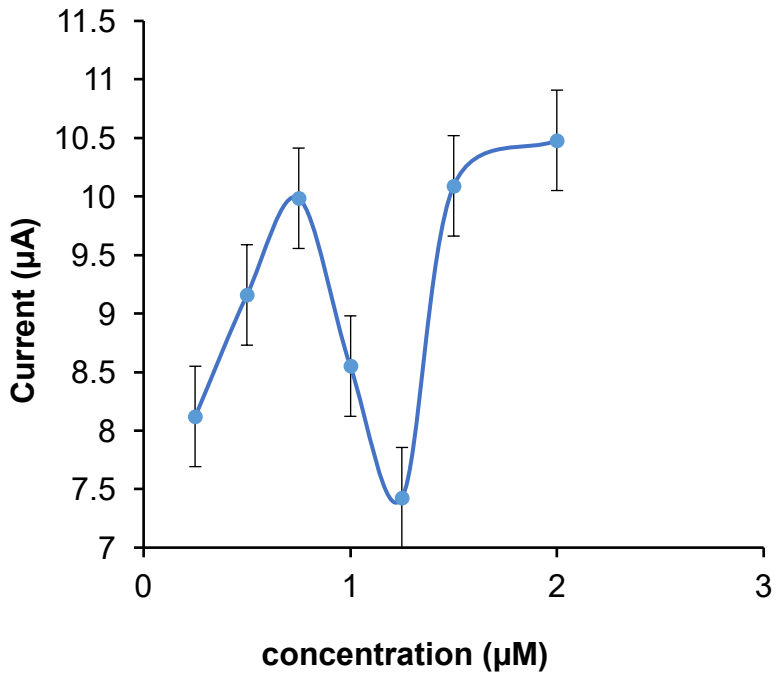

Figure 2.1: Plot of current versus concentration of an aptamer on top of complex **1** (0.25-2.0 µM) from Cycliclic voltammograms done in 0.1 M KCl containing 1 mM $[Fe(CN)_6]^{3-/4-}$ solution.

Please note that ads (adsorbed) of the aptamer are only used for electrodes containing complexes **3** and **4** to differentiate from covalent (cov) bonding discussed below. Complexes **3** and **4** have COOH, which allows them to be covalently linked into aptamer as follows. DCC (6.0 mg, 0.029 mmol) and NHS (4.0 mg, 0.035 mmol) were added to the electrodes containing complexes **3** and **4**. The electrodes were then left to stand at room temperature for 1 h. Then, the aptamer (5 µL, 0.75 µM) was dropped on the DCC/NHS activated surfaces to allow for the carboxylic group rich in CoPc to interact with the amine group of an aptamer to give: GCE-(**3**)-aptamer(cov), GCE-(**4**)-aptamer(cov), GCE-EG-(**3**)(seq)-aptamer(cov), GCE-EG-(**4**)(seq)-aptamer(cov), GCE-EG-(**3**)(π-π)-aptamer(cov), GCE-EG-(**4**)(π-π)-aptamer (cov), where cov represents covalent bonding of an aptamer (**Scheme 4.1**). A complete list of electrodes may be found in **Table 4.1**.

The electrodes containing aptamer were used to detect PSA using electrochemical impedance spectroscopy (EIS) and differential pulse voltammetry (DPV). Before running EIS and DPV, the electrodes were incubated for 30 min in a solution of $[Fe(CN)_6]^{3-/4-}$ (1 mM in 0.1M KCl) in PBS (PH 7.4) at different PSA concentrations at room temperature. EIS experiments were performed in a frequency range from 0.1 Hz to 100 kHz, using 0.01 V_{RMs} sinusoidal modulation. A non-linear least square (NLLS) method based on the EQUIVCRT program was used for the automatic fitting of the obtained EIS data.

Publications

The results presented in the following chapters are in the articles below that have been published or in preparation for publication in peer-reviewed journal. These are articles are not referenced in this thesis

1. E. Benise, T. Nyokong, Electrochemical detection of prostate specific antigen in the presence of an aptamer and composites of cobalt phthalocyanine-exfoliated graphite, Polyhedron (**2023**) 116674.

2. E. Benise, L.S. Mpeta, T. Nyokong, Aptamer-Based Biosensor for Prostate Specific Antigen Detection Using Cobalt Phthalocyanine-Exfoliated Graphite Composite, In preparation.

Chapter 3: Synthesis and Characterization

This is the chapter about the synthesis, and characterization of EG, CoPc (1), (2), (3) and (4) as well as EG-1 (π-π), EG-2 (π-π), EG-3 (π-π), EG-4 (π-π) conjugates.

3.1. MPc synthesis and characterization

Scheme 3.1 shows the synthesis of the new complexes **3** and **4**. The synthesis of complex **3** and complex **4** is from the statistical condensation of phthalonitrile **A** with either phthalonitriles **B** or **C**. The percentages obtained from the elemental analyses suggest that the complexes are hydrates, which have been reported to be the case for some Pcs [**83**]. Mass spectra gave the expected results in which the obtained mass for complex **3** was 1155.82 m/z, **Fig.A1** (Appendix), whereas in complex **4**, it was 1182.76 m/z, **Fig.A2** (Appendix). Nuclear magnetic resonance spectra were not recorded due to the paramagnetic nature of central metal (Co). Complexes **1** and **2** are known and gave statistically analysis data in Appendix. The further characterization of MPc is UV-Vis spectra.

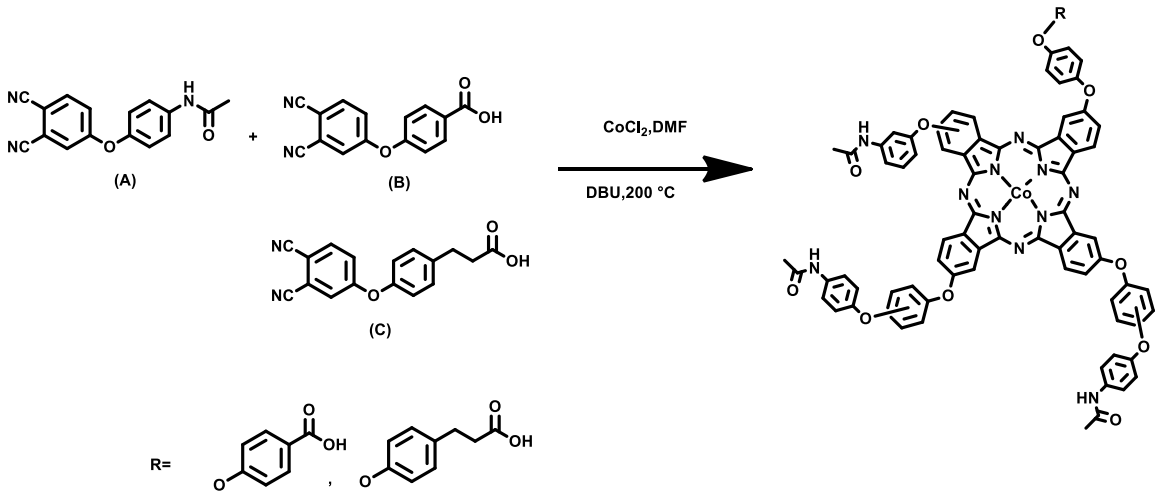

Scheme 3.1: Synthesis of CoPc complexes **1**, **2, 3** and **4**.

The UV-Vis absorption spectra of the four CoPc complexes are shown in **Fig. 3.1**. UV-Vis was done to check the presence of Q and B bands in the complexes. The Q bands for CoPc complexes **1**, **2, 3**, and **4** were respectively found at 665 nm, 661 nm, 664 nm, and 662 nm (**Table 3.1**), and this is typical for CoPcs [**84**]. In addition, the B bands for the complexes were found at 321 nm, 323 nm, 323 nm, and 321 nm (**Table 3.1**).

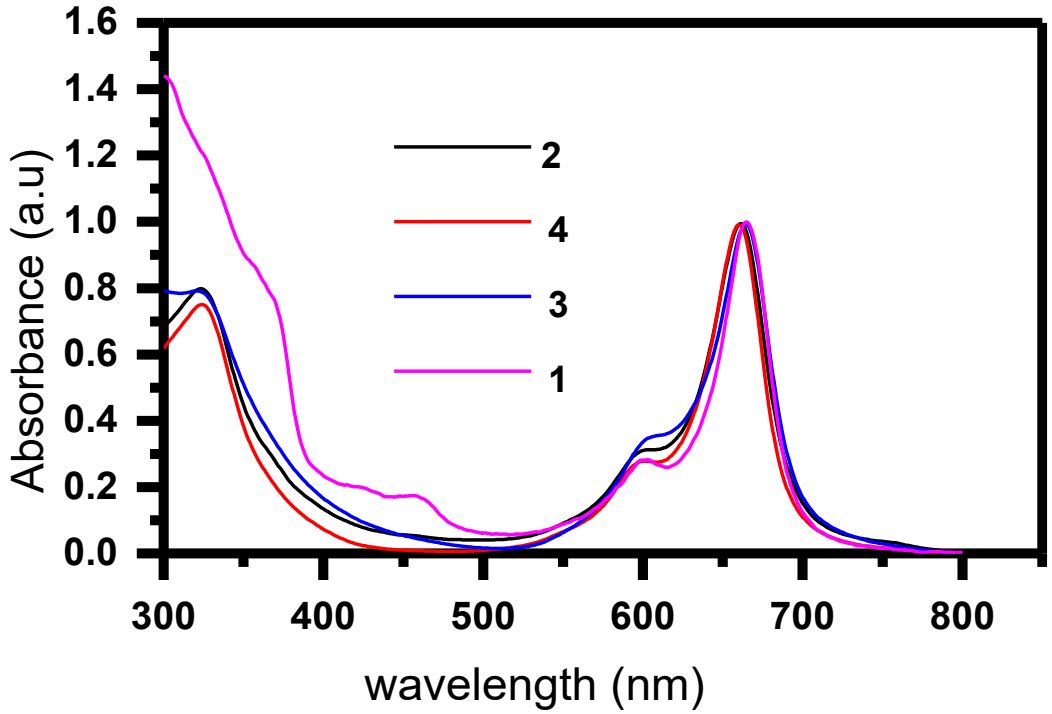

Figure 3.1: UV-Vis spectra of CoPc complexes **1**, **2, 3** and **4**.

Table 3.1: Q bands of UV-Vis complexes; **1**,**2**,**3**,**4** and the pi-pi stacked EG with each complex in DMSO.

Complex/conjugate	λ_{max} (Q band)
1	665
2	661
3	664
4	662
EG (**1**)(π-π)	677
EG (**2**)(π-π)	662
EG-(**3**)(π-π)	665
EG-(**4**)(π-π)	669

3.2. Synthesis of EG and characterization

Scheme 3.2 shows the synthesis of exfoliated graphite by acid treatment of the starting material natural graphite flakes (NGF) and heating the intermediate product in the preheated furnace. The characterization techniques used for NGF and EG were XRD, TGA, BET, and SEM-EDS. The two materials were characterized together using the above characterization techniques to study the effects of exfoliation.

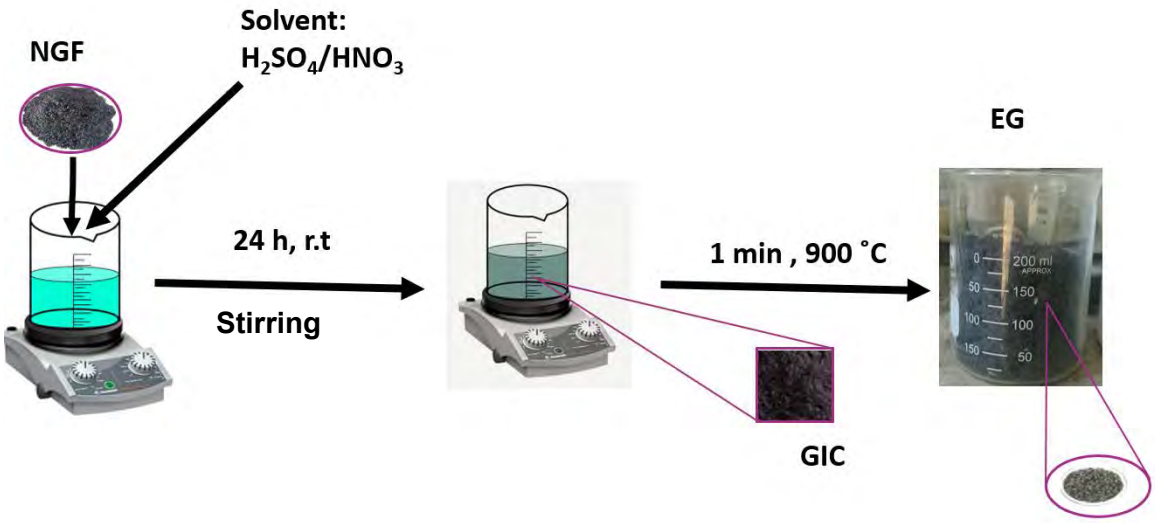

Scheme 3.2: Synthesis of EG.

3.2.1. X-ray diffraction microscopy (XRD) and Thermogravimetric Analysis (TGA) of NGF and EG

The two characterization techniques, XRD and TGA, were done to show the crystallographic structure and the thermal stability of NGF and EG. NGF has well-defined peaks at 2θ = 27˚ and 2θ = 55˚, and these peaks correspond to (002) and (004) diffractions, respectively (**Fig. 3.2(a)**). The two diffraction peaks are characteristic of a pure crystalline NGF [**85**]**.** EG has the same peaks at the same positions. The similarity of the XRD patterns for EG and NGF shows that the elementary constituent did not undergo any change after exfoliation [**86**]. In TGA (**Fig. 3.2(b**)), the decompositions of NGF and EG occur after 700 ˚C, and this is due to carbon being oxidized to carbon dioxide [**87**].

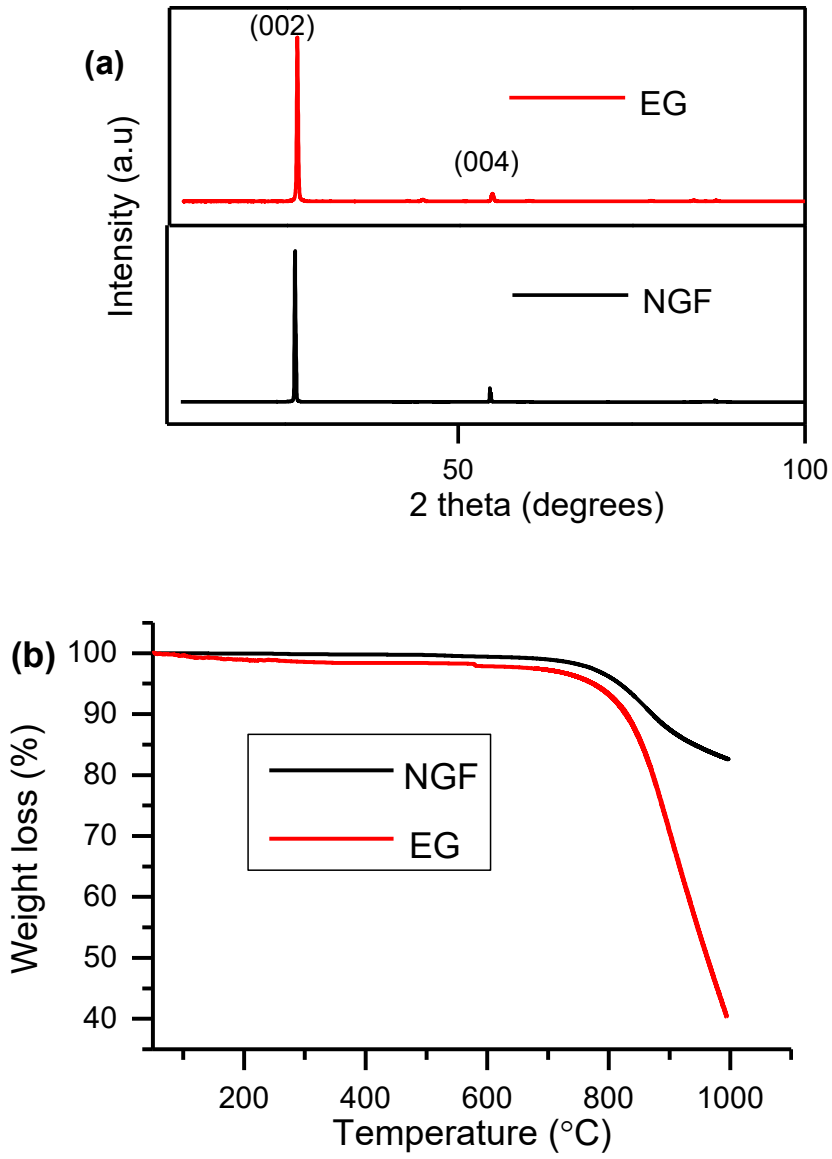

Figure 3.2: (a) X-ray diffraction (XRD) analysis of NGF and EG, and (b) TGA plots of NGF and EG in the nitrogen atmosphere at heating rates of 10 °C min^{-1}.

3.2.2. Scanning electron microscopy-energy dispersive spectroscopy (SEM-EDS) images

Fig. 3.3 (a) shows SEM and EDS images of natural graphite flakes (NGF), and **Fig. 3.3(b)** of exfoliated graphite (EG). The NGF has flake-like structures that are agglomerated or are close to each other, with a surface that is flat and uniform [31].

EG has an accordion-like structure with expanded layers that are packed regularly [25]. **Fig. 3.3** also shows the elemental composition of NGF and EG, where there is only the presence of carbon for both NGF and EG (**Fig. 3.3 (a), (b)**). Graphite is known as the naturally occurring form of carbon [87].

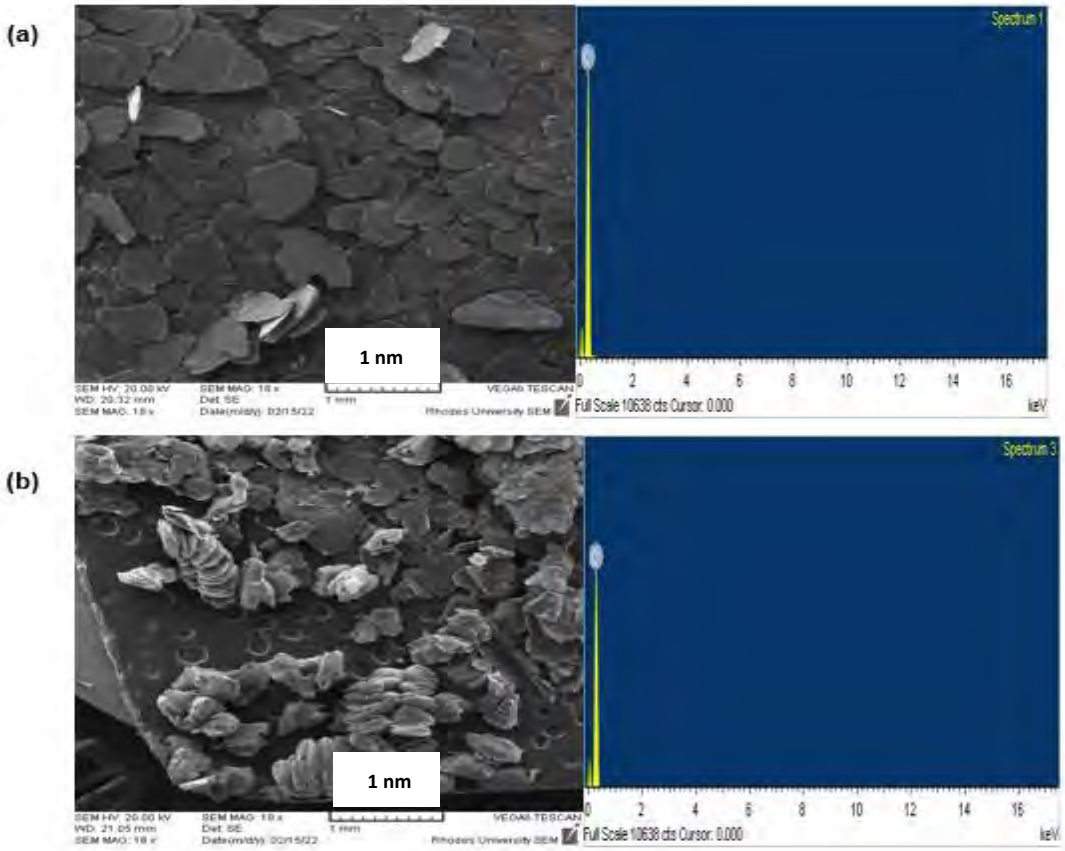

Figure 3.3: SEM (left) –EDS (right) images of (a) NGF and (b) EG.

3.2.3. Brunner Emmet Teller (BET) analysis

The adsorption/desorption isotherms are used to determine the desorption average pore diameter and BET surface area of NGF and EG (**Fig. 3.4**). The type of i sotherm observed for NGF is a type I characterized by micropores. EG exhibits a mixture of type II and type IV. EG isotherm is also characterized by a small desorption branch, primarily associated with mesopore [86]. The pore diameter and BET surface

area of NGF and that of EG were respectively 48.185 Å and 132.264 Å, 0.3552 m^2/g, and 16.0399 m^2/g. The increase in BET surface area and pore diameter from NGF to EG show that EG is more likely to adsorb phthalocyanine dye than NGF [88].

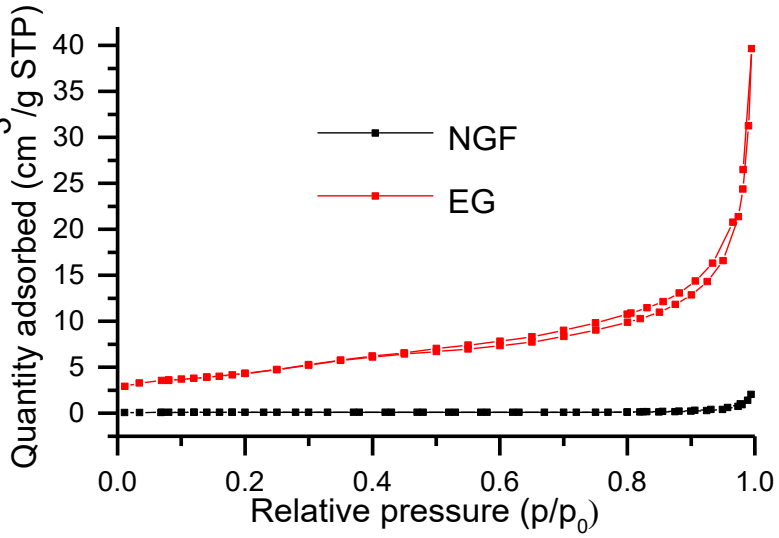

Figure 3.4: BET plots of the NGF and EG.

3.3. Characterization of MPc-EG composites

MPc has π- electrons, which allows them to be π-π stacked with other materials. In this work, each complex of CoPc was π-π stacked with EG in **Scheme 3.3** (CoPc **1** was used as an example). The characterization techniques SEM-EDS, TGA, and XRD for the composite (EG-CoPc (π-π)) did not show any difference compared to EG due to the small amount of the Pc; hence these are not shown. Characterization of the MPc-EG composites was by UV-Vis and Raman spectra.

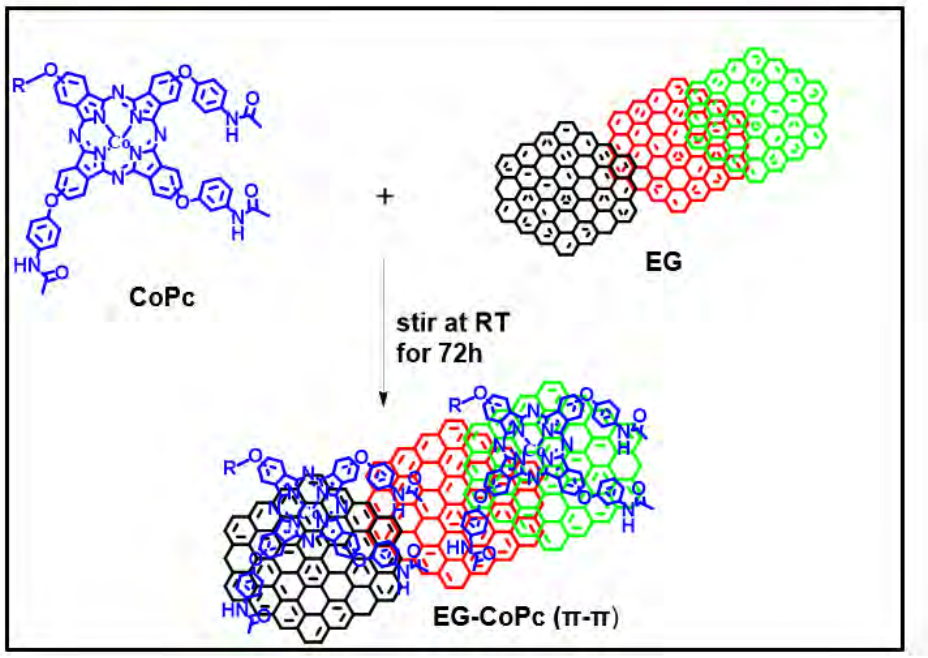

Scheme 3.3: Illustration of π-π stacking of complex 1 onto EG (π-π)) as an example.

3.3.1. UV-Vis Spectra

The conjugation of EG with CoPc complexes resulted in the shift of the Q and B bands that were observed for the complexes using UV-Vis spectra (**Fig. 3.5**). Except for complexes **1** and **4**, the Q bands of the complexes **2** and **3** did not change or shift significantly following π- π stacking onto EG, **Table 3.1**. A slight red shift of the Q was observed for complexes **1** and **4**. The red shift of the Q band might be due to the intercalation of CoPc into carbon sheets of EG due to the strong π-π interaction between CoPc and EG [89]. In addition, the literature states that the red shift of the Q band in porphyrin–graphene oxide nanoconjugates is caused by molecular flattening [89].

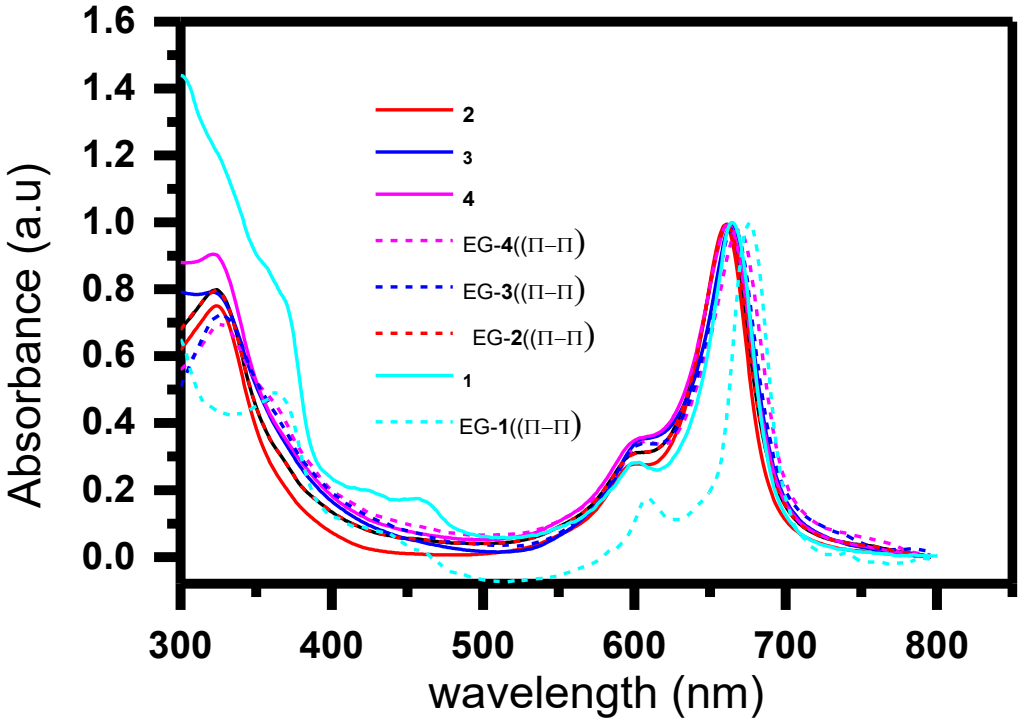

Figure 3.5: (a) UV-Vis of **1**, EG-**1** (π-π) and (B) **2**, **3**, **4**, EG-**2** (π-π), EG-**3** (π-π), EG-**4** (π-π).

3.3.2. Raman spectra

Fig. 3.6 (a) shows the Raman spectrum of CoPc which is characterized by three vibration bands. These Raman peaks have been observed before for Pcs [**90**]. The Raman spectrum of pure graphite is characterized by a first-order band in the range of 200-2000 cm^{-1} and a second order at 2000-3400 cm^{-1} [**91**] (**Fig. 3.6(b)**). In the graphitic structure, in-plane vibrations of sp^2-bonded carbon atoms result in the G band. In contrast, the D band results from out-of-plane vibrations due to structural defects (sp^3 carbons).

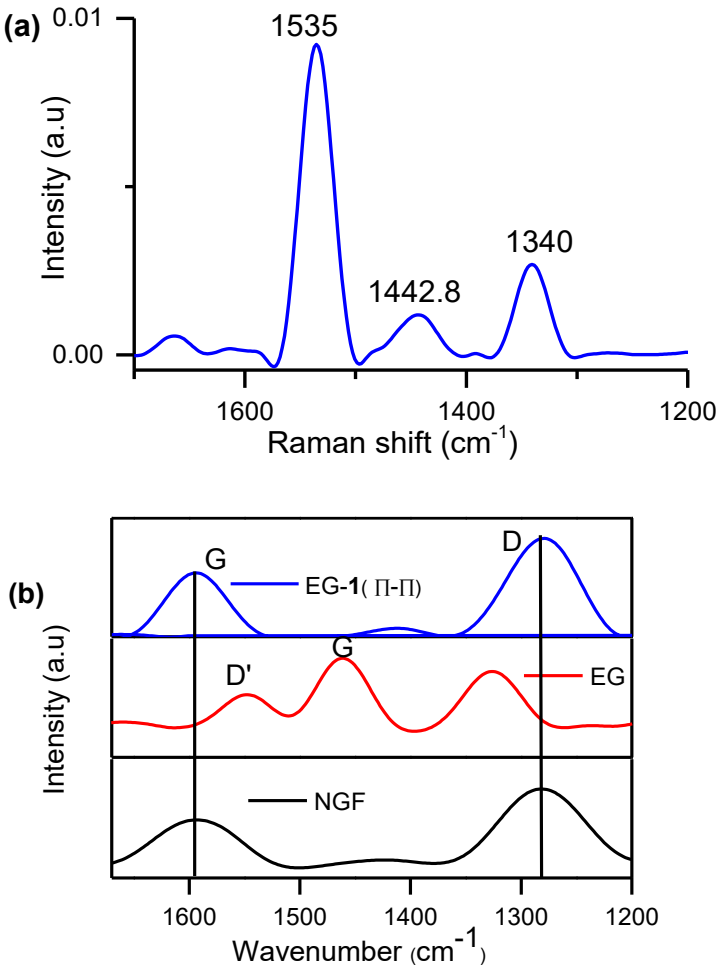

Figure 3.6: Raman spectra of (a) **1** and (b) NGF, EG and EG-**1** (π-π)

1st order peaks are normally observed at about 1350 cm^{-1} (D-band), 1590 cm^{-1} (G-band), and 1620 cm^{-1} (D'-band) [92]. The D' band corresponds to an intra-valley resonance with the G band and occurs at the higher wavenumber side of the G band [92]. In (**Fig. 3.6(b)**) and **Table 3.2**, the D and G bands of NGF were found at about 1280 (D), 1583 cm^{-1} (G). The bands for EG were respectively found at about 1317 cm^{-1} (D) and 1456 cm^{-1} (G), and a D' band was also found at around 1579 cm^{-1} (**Fig. 3.6(b)**). D and G bands of EG-CoPc (π-π) were found at about 1282 cm^{-1} and 1579 cm^{-1} (**Fig. 3.6(b)**). The rest of CoPc (π-π) data is in **Table 3.2**. The peaks due to the Pc (especially the intense one at 1535 cm^{-1}) are not observed in the Raman spectrum

of EG-**1**(π-π) due to the small amounts of the Pc. The D' band was not visible on NGF and EG-**1** (π-π). The D band (the disorder band) is higher in intensity than the G band in some cases. The high intensity of the D band has been associated with many factors, including synthesis temperature [92]. The intensity ratio of the two bands, D and G peaks (I_D /I_G) is related to the number of defects in the material. The calculated I_D/I_G values are as follows: NGF= 1.14, EG = 0.7 and EG-**1**(π-π) = 1.01, EG-**2**(π-π) = 1.01 EG-**3**(π-π) =1.1, EG-**4**(π-π) = 1.14 (**Table 3.2**). NGF and EG-CoPc (π-π) showed I_D/I_G ratios greater than 1. The I_D/I_G ratios of EG-CoPc (π-π) are higher than the I_D/I_G ratio of EG, showing that the π-π stacking resulted in an increase in defects [92].

Table 3.2: Raman data of NGF, EG, EG- (**1**)(π-π), EG- (**2**)(π-π), EG- (**3**)(π-π), and EG-(**4**)(π-π).

Material / conjugate	D band	G	(I_D /I_G)
NGF	1280	1583	1.14
EG	1317	1456	0.70
EG (**1**)(π-π)	1282	1579	1.01
EG (**2**)(π-π)	1348	1543	1.01
EG-(**3**)(π-π)	1346	1599	1.10
EG-(**4**)(π-π)	1381	1532	1.14

3.4. Conclusions

The information obtained from spectroscopic and microscopic techniques successfully confirmed the synthesis of this work's synthesized compounds, which are CoPc complexes, EG, and EG-CoPc (π-π) conjugates. Mass spectra, elemental analysis, UV-Vis, and Raman spectra were successfully employed for all 4 complexes. EG was characterized using SEM-EDS, Raman spectra, TGA, XRD, and BET. To confirm π-π staking of EG to the complexes, Raman spectra and UV-Vis spectra were employed successfully.

Chapter 4: CHARACTERIZATION OF THE MODIFIED ELECTRODES

This chapter examines the electrochemical methods used to characterize a modified glassy carbon electrode (GCE) in ferricyanide and phosphate buffer saline (PBS) for electron transfer.

4.1. Characterization in ferricyanide solution

4.1.1. Cyclic voltammetry (CV)

Ferricyanide is a known redox probe for the characterization of GCE. The choice is motivated by the high reversibility and stability of this probe [93]. CV studies (**Fig. 4.1 (a)** using complex **1** and its EG composites (were used as representatives), and were carried out in a solution of 1mM $[Fe(CN)_6]^{3-/4-}$ in 0.1M KCl. The anode-to-cathode peak potential difference (ΔEp) values are listed in **Table 4.1**). The ΔEp of bare of GCE (at 80 mV) is closer to the Nernstian value for a one-electron process, and this serves as an indication of their excellent charge transfer kinetics for the $[Fe(CN)_6]^{3-/4-}$ in KCl. A lower value of ΔEp means a better charge transfer process. ΔEp values decreased in the presence of EG compared to corresponding CoPc complexes alone due to enhanced charge transfer. The peak potential differences of sequentially modified electrodes containing both CoPcs and EG to make GCE-EG-(**1**) (seq), GCE-EG-(**2**) (seq), GCE-EG-(**3**) (seq) and GCE-EG-(**4**) (seq) were found to be smaller than ΔEp for GCE-EG-(**1**)(π-π), GCE-EG-(**2**)(π-π), GCE-EG-(**3**)(π-π) and GCE-EG-(**4**)(π-π) (**Table 4.1)**. This shows that the electrode works best when the CoPc is placed on top of EG. The solution to run the electrodes with an aptamer was 1 mM $[Fe\ (CN)_6]^{3-/4-}$ prepared in a 30 mM phosphate buffer saline of pH 7.4. The modification of GCE followed by the covalent linking or adsorption of an aptamer is shown in **Fig 4.1**, **Table 4.1** and **Scheme 4.**1. Aptamer was covalently linked to complexes **3** and **4** containing electrodes. Complexes **3** and **4** have COOH groups, which form a covalent (amide) bond with NH_2 of an aptamer. The peak potential differences of covalently linked

aptamer for GCE-(**3**)-aptamer(cov), GCE-EG-(**3**)(seq)-aptamer(cov), GCE-EG-(**3**)(π-π)-aptamer(cov), GCE-(**4**)-aptamer(cov), GCE-EG-(**4**) (seq)-aptamer(cov), were generally found to be smaller than when the aptamer was adsorbed for the corresponding GCE-(**3**)-aptamer(ads), GCE-EG-(**3**)(seq)-aptamer(ads), GCE-EG-(**3**)(π-π)-aptamer(ads), GCE-(**4**)-aptamer(ads), and GCE-EG-(**4**)-aptamer(ads). This shows that the covalent linking of the aptamer to the complexes resulted in an increase in specific binding between COOH of the CoPc and NH_2 of an aptamer. ΔEp of GCE-EG-(**4**)(π-π)-aptamer(ads) and GCE-EG-(**4**)(π-π)-aptamer(cov) were the same.

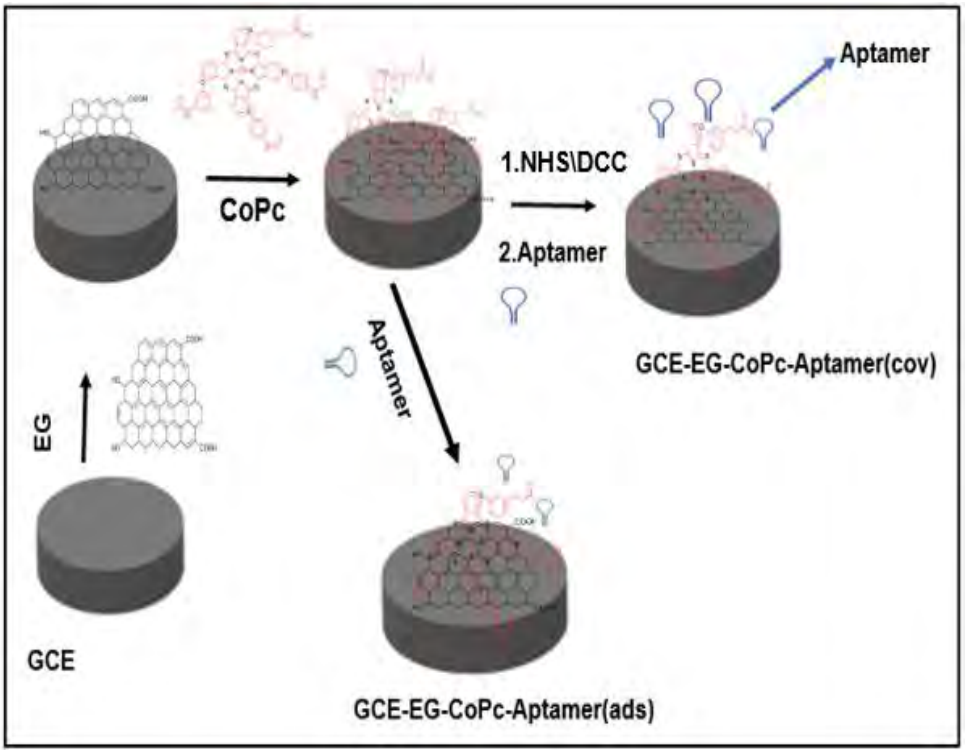

Scheme 4.1: Represent the GCE to GCE-EG-**4**-aptamer (adsorbed)/ and (covalently linked).

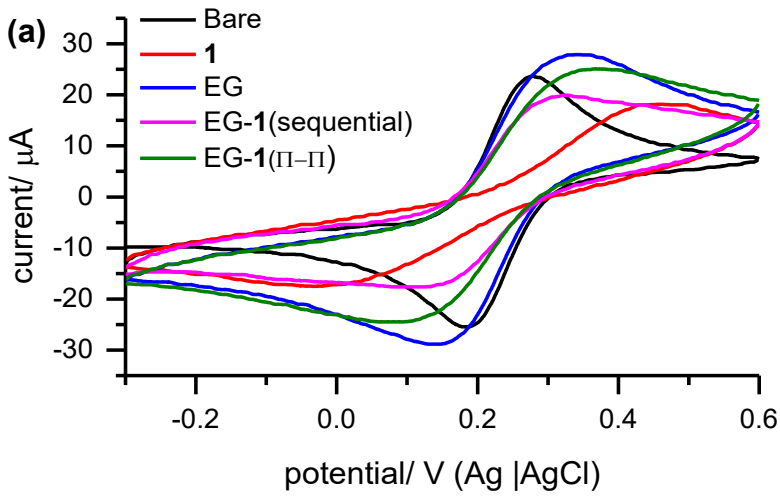

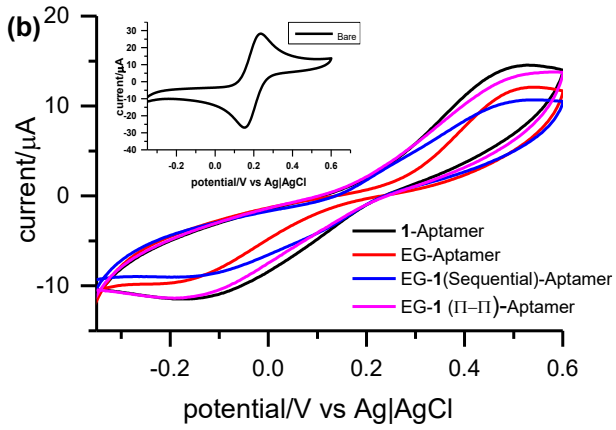

Figure 4.1: CV of (a) Bare, GCE-**1**, GCE-EG, GCE-EG-**1**(seq), GCE-EG-**1**(π-π) in 0.1 M KCl containing 1 mM $[Fe(CN)_6]^{3-/4-}$ solution; Scan rate=100 mV/s. (b) **1**-Aptamer, EG-Aptamer, EG-**1**(sequential)-Aptamer, EG-**1**(π-π)-Aptamer (insert: Bare) 0.1 M KCl containing 1 mM $[Fe(CN)_6]^{3-/4-}$ in 0.03 M phosphate buffer saline of pH 7.4.; Scan rate= 100 mV.

4.1.2. Electrochemical impedance spectroscopy (EIS)

EIS studies were also carried out in 1 mM $[Fe(CN)_6]^{3-/4-}$ in 0.1M KCl solution as an alternative technique of CV to understand charge transfer kinetics resistance (R_{ct}) occurring at the electrode/electrolyte interface (**Fig. 4.2 (a)**, using complex **1** as a representative). The Randles fitting model (**Fig. 4.2(c)**) was used to fit the EIS data since a well-defined semi-circle was observed. This model includes the solution resistance (R_s), the charge transfer resistance (R_{ct}), the double-layer capacity element (Cdl), and a Warburg element (Z_W). The electrodes in the presence of an aptamer were run in 1 mM $[Fe\ (CN)_6]^{3-/4-}$ prepared in a 30 mM phosphate buffer saline of pH 7.4 from which the electrodes of complex **1** are used as representatives (**Fig. 4.2 (b)**). Except for GCE-EG-(**2**)(seq) and GCE-EG-(**2**)(π-π) in the absence of the aptamer, R_{ct} values for sequentially modified were found to be smaller than the R_{ct} values of the π-π stacked composite in the absence or presence of the aptamer (**Table 4.1**), hence a better charge transfer for the former. The R_{ct} values in the presence of an aptamer were found to generally decrease when the aptamer was covalently linked to complexes **3** and **4**, corresponding to ΔEp values (**section 4.1.1**.). The decrease in R_{ct} values is due to increased specific binding between the CoPc and an aptamer.

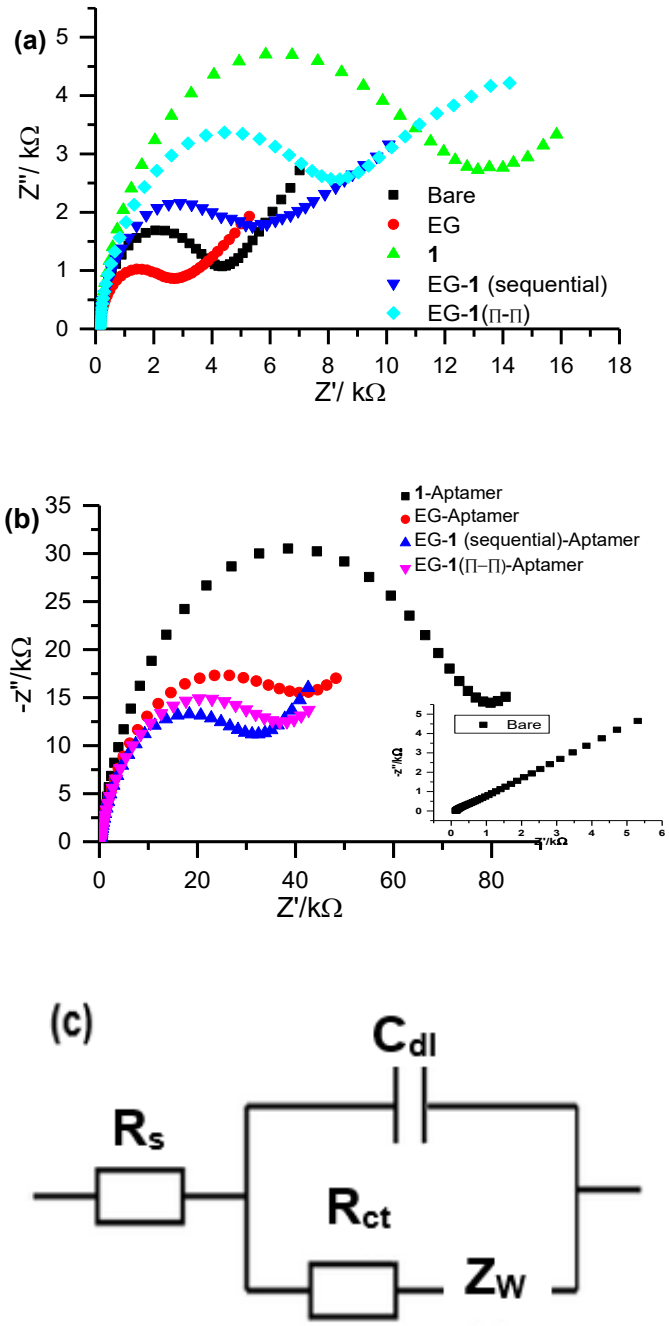

Figure 4.2: (a) Electrochemical impedance (EIS) Nyquist plots of **1**, EG, EG-**1**(sequential) and EG-**1**(π-π), (b) **1**-Aptamer, EG-Aptamer, EG-**1**(sequential)-Aptamer and EG-**1**(π-π)-Aptamer (Bare) (Insert: Bare- Aptamer), (c) a Randles fitting model used in (a) 0.1 M KCl containing 1 mM [Fe $(CN)_6$]3−/4, and (b) 0.1 M KCl containing 1 mM $[Fe(CN)_6]^{3-/4-}$ prepared in 0.03 M phosphate buffer saline of pH 7.4; Scan rate= 100 mV.

Table 4.1: Summary of electrochemistry parameters for the bare and modified electrodes in (a) 0.1 M KCl containing 1 mM $[Fe(CN)_6]3-/4$, and (b) 0.1 M KCl in 1 mM $[Fe(CN)_6]^{3-/4-}$ prepared in 0.03 M phosphate buffer saline of pH 7.4.

Complex	**ΔEp(mV)**	**R_{ct}(KΩ)**
GCE-Bare	80.0	18.0
GCE-EG	497	23.2
GCE-(1)	450	9.14
GCE-(2)	554	175
GCE-(3)	551	420
GCE-(4)	518	164
GCE-EG(seq)-(1)	174	4.31
GCE-EG(seq)-(2)	298	20.7
GCE-EG(seq)-(3)	351	0.0170
GCE-EG(seq)-(4)	385	0.0250
GCE-EG-(1)(π-π)	284	6.25
GCE-EG-(2)(π-π)	356	0.150
GCE-EG-(3)(π-π)	491	0.240
GCE-EG-(4)(π-π)	487	0.100
GCE-aptamer	334	2.20
GCE-EG-aptamer	225	54.3
GCE-(1)-aptamer	623	74.2
GCE-(2)-aptamer	529	140
GCE-(3)-aptamer(ads)	515	43.5

GCE-(4)-aptamer(ads)	537	13.0
GCE-EG-(1)(seq)-aptamer	550	30.2
GCE-EG-(2)(seq)-aptamer	247	54.4
GCE-EG-(3)(seq)-aptamer(ads)	471	30.2
GCE-EG-(4) seq)-aptamer(ads)	240	0.0810
GCE-EG-(1)(π-π)-aptamer	598	35.8
GCE-EG-(2)(π-π)-aptamer	281	74.8
GCE-EG-(3)(π-π)-aptamer(ads)	542	105
GCE-EG-(4)(π-π)-aptamer(ads)	277	58.9
GCE-(3)-aptamer(cov)	513	25.2
GCE-(4)-aptamer(cov)	431	0.670
GCE-EG-(3)(seq)-aptamer(cov)	321	23.1
GCE-EG-(4)(seq)-aptamer(cov)	237	0.470
GCE-EG-(3)(π-π)-aptamer(cov)	417	32.5
GCE-EG-(4)(π-π)-aptamer(cov)	277	28.1

Bare = electrode without modification

4.2. Characterization in 0.03 M phosphate buffer saline (PBS)

The modified electrodes in the presence of an aptamer were tested for CV (complex **1** electrodes were used as representatives). The PBS buffer was used as a blank to distinguish the activity in the absence of the redox mediator ($[Fe(CN)_6]^{3-/4-}$). No peaks were observed for CoPc (**Fig. 4.3).** This shows that the use of the redox mediator ($[Fe(CN)_6]^{3-/4-}$) in this work was of advantage.

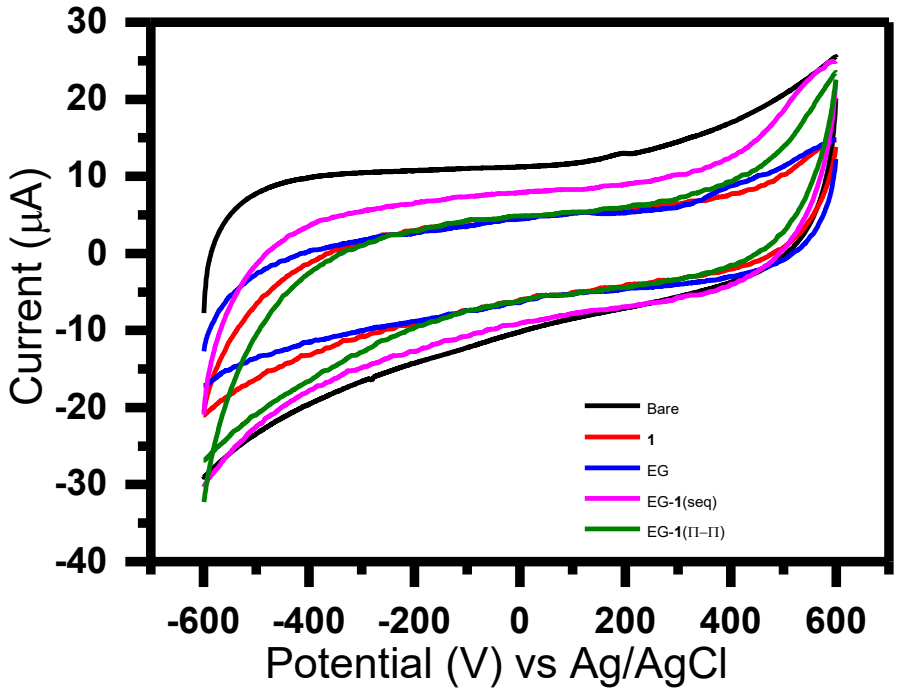

Figure 4.3: CV of bare, CoPc, EG, CoPc-EG (sequential), and CoPc-EG (π- π-) in 0.03 M PBS solution of pH 7.4. Scan rate 100 mV (starting potential of scans =-600 mV).

4.3. Summary of the chapter

The CV diagrams were obtained in 1mM $[Fe(CN)_6]^{3-/4-}$ in 0.1M KCl and 1 mM $[Fe(CN)_6]^{3-/4-}$ in 0.1 M KCl prepared in a 30 mM phosphate buffer saline of pH 7.4 solutions showed the difference in electron transfer abilities of the probe. The CoPc alone showed poor electron transfer ability, which improved when EG was introduced. The varying ΔEp values indicate that the modification was successful. Electrochemical impedance spectroscopy further proves this since most R_{ct} values correspond with CV results studies. The covalent linking of an aptamer in complex **3** and complex **4** electrodes resulted in better electron transfer of the electrodes compared to when an aptamer was adsorbed in these electrodes for both CV and EIS. The ability to observe the peaks on the CV of the modified electrodes was due to the redox

mediator presence with PBS since no peaks were observed when only PBS was used as a solution for CV.

Chapter 5: Detection of PSA

The discussion of this chapter is about the electrochemical detection of a prostate specific antigen (PSA).

5. Detection of the prostate specific antigen (PSA)

5.1. Concentration studies using electrochemical impedance spectroscopy and differential pulse voltammetry

In detecting the PSA, concentrations of PSA ranging from 1.0 to 2.0 pM were used. The electrodes that were used for the detection of PSA were the ones that had an immobilized aptamer. GCE-EG-(**4**)-aptamer(ads) was used as a representative in **Fig. 5.1**. The calibration plot (insert in **Fig. 5.1 (a)**) shows that the plots R_{ct} of GCE-EG-(**4**)-aptamer(ads) at different concentrations of PSA were linear. This plot was used to calculate the limit of detection (LoD), equation 5.1, with values listed in **Table 5.1**. The smaller the value of LoD, the better the electrode in detecting the PSA.

$$\text{LoD} = \frac{3\sigma}{\text{sensitivity}} \qquad (5.1)$$

Where sensitivity is the gradient of the calibration curve and σ is a standard deviation of the blanks (the electrode ran 15 times for DPV and EIS, in the absence of PSA). Using EIS, GCE-**3**-Aptamer (ads) and GCE-**4**-Aptamer(ads) have a lower LoD value than GCE-**1**-Aptamer and GCE-**2**-Aptamer which shows that asymmetrical substitution improves LoD. In the presence of EG, the LoD improved when compared to CoPc complexes alone. Comparing sequentially modified electrodes with π-π stacked CoPc and EG and with the aptamer adsorbed, the former gave lower LoD, maybe because the CoPc is on top. The same applies when the aptamer is covalently linked. The electrodes where the aptamer is covalently attached: GCE-EG(**3**)-aptamer(cov), (**4**)-aptamer(cov) showed lower LoD values than when the aptamer is adsorbed in GCE-EG(**3**)-aptamer(ads), GCE-(**4**)aptamer(ads), because covalent linking the complexes to aptamer was specific when compared to adsorption. The literature LoD values obtained in this work for the detection of PSA were, in general,

better than the values obtained in literature at 0.031 ng/mL for GCE-gCNQDs@aptamer-(**5**) (gCNQDs= graphitic carbon nitride quantum dots), 0.023 ng/mL for GCE-gCNQDs@aptamer-(**6**) [74], 0.044 ng/mL, 0.026 ng/mL and 0.14 ng/mL for the reported NGQDs-CoPc**7**-Aptamer (NGQDs = nitrogen doped graphene quantum dots), GCE-AuNPs-CoPc**8**-Aptamer (NP = nanoparticle), and SPE-GQDs-AuNRs (SPE = screen printed electrode; NR = nanorods) [73, 75, 94], respectively, **Table 5.1**. The DPV results are illustrated in **Fig. 5.1 (b)**, where a peak around 0.3 V was observed, and this peak was also observed in the literature [95].

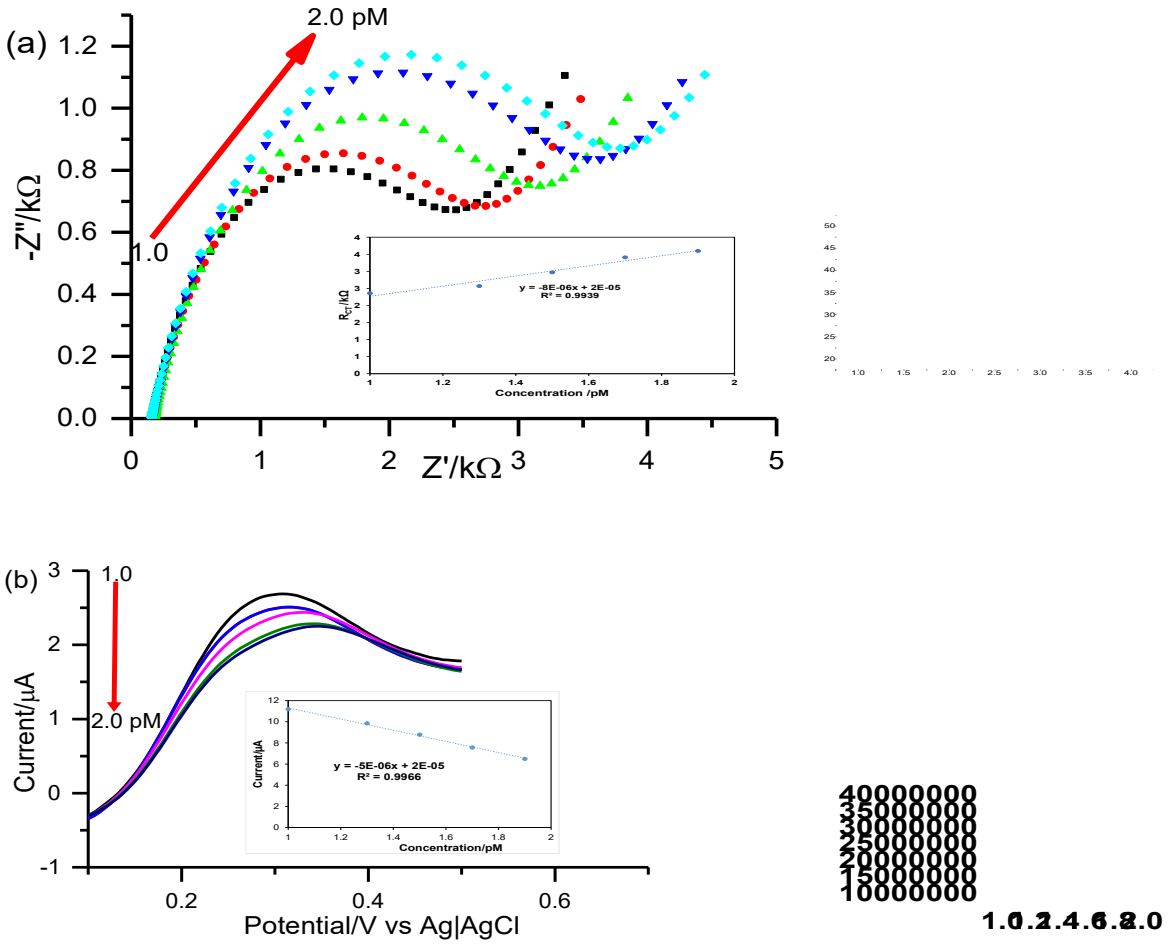

Figure 5.1: (a) Electrochemical impedance (EIS) Nyquist plots and (b) DPV plots in 0.1 M KCl containing 1 mM $[Fe(CN)_6]^{3-/4-}$prepared in a 30 mM phosphate buffer saline

of pH 7.4 of GCE-EG-(**4**)-aptamer (ads) with PSA concentration ranging from 1.0-2.0 pM.

Table 5.1: Summary of the LoDs obtained from EIS and DPV in the concentration range (1.0 to 2.0) of PSA. The units of LoD values from this work were converted from pM to ng/ml to be compared with the literature.

Sample	**Linear range ng/mL**	**LoD (EIS)/ ng/mL**	**LoD (DPV)/ ng/mL**	**Reference**
GCE-EG-aptamer	0-0.068	0.0342	0.000162	This work
Complex **1**				
GCE-(**1**)-aptamer	0-0.068	0.43	8.28	This work
GCE-EG-(**1**)(seq)-aptamer	0-0.068	0.0011	0.0033	This work
GCE-EG-(**1**)(π-π)-aptamer	0-0.068	0.0017	0.017	This work
	Complex **2**			
GCE-(**2**)-aptamer	0-0.068	0.280	0.280	This work
GCE-EG-(**2**)(seq)-aptamer	0-0.068	0.00651	0.00456	This work
GCE-EG-(**2**)(π-π)-aptamer	0-0.068	0.00708	0.00877	This work
Complex **3**				
GCE-(**3**)-aptamer(ads)	0-0.068	0.193	0.193	This work
GCE-(**3**)-aptamer(cov)	0-0.068	0.00133	0.00708	This work
GCE-EG-(**3**)(seq)-aptamer(ads)	0-0.068	0.00315	0.00901	This work

GCE-EG-(**3**)(seq)-aptamer(cov)	0-0.068	0.00262	0.00823	This work
GCE-EG-(**3**)(π-π)-aptamer(ads)	0-0.068	0.00921	0.0133	This work
GCE-EG-(**3**)(π-π)-aptamer-(cov)	0-0.068	0.0032	0.0078	This work
Complex **4**				
GCE-(**4**)-aptamer(ads)	0-0.068	0.0214	0.00958	This work
GCE-(**4**)-aptamer(cov)	0-0.068	0.0101	0.00265	This work
GCE-EG-(**4**)(seq)-aptamer(ads)	0-0.068	0.00710	0.00183	This work
GCE-EG-(**4**)(seq)-aptamer(cov)	0-0.068	0.00103	0.00148	This work
GCE-EG-(**4**)(π-π)-aptamer(ads)	0-0.068	0.00718	0.00825	This work
GCE-EG-(**4**)(π-π)-aptamer(cov)	0-0.068	0.00166	0.00560	This work
GCE-gCNQDs@aptamer-CoPc (**5**)	0.048-0.068	0.0310	-	[74]
GCE-gCNQDs@aptamer-CoPc (**6**)	0.048-0.068	0.023	-	[74]

GCE-NGQDs-CoPc**7**-Aptamer	0.034-0.057	0.044	-	[73]
GCE-AuNPs-CoPc**8**-Aptamer	1.2-2.0	0.026	0.028	[75]
SPE-GQDs-AuNRs	0.14-11	0.14	0.14	[94]

gCNQDs= graphitic carbon nitride quantum dots, CoPc (**5**) = 2-benzoic acid-9(10),16(17),23(24)-tris(2,6-di-tert-butyl-4-methylphenoxy)phthalocyaninato cobalt (II) (1): CoPc (**6**) = 2-N,N"-hex5-yn-1-yloxy)-9(10),16(17),23(24)-tris(benzene-4,1-diyl))triacetamide phthalocyaninato cobalt(II), ads = adsorbed, cov=covalent, NGQDs= nitrogen doped graphene quantum dot, AuNPs= gold nanoparticles, GQDs-AuNRs = graphene quantum dots gold nanorods. SPE = screen printed electrode, CoPc**7** = mono(carboxyphenoxy)-tri(2,6-di-tert-butyl-4-methylphenoxy) Co (II)phthalocyanine: CoPc**8** = N, N′, N''-(((23-(hex-5-yn-1-yloxy)-2(3),9(10),16 (17)-triyl)tris(oxy))tris(benzene-4,1-diyl))triacetamide phthalocyaninato cobalt (II).

Using DPV, linear responses of current with change in concentration of PSA were also observed where the peak current decreased with an increasing PSA concentration. The reason for this is that the immobilized aptamer undergoes conformational change due to the binding with PSA [96]. LoD was also calculated using equation 5.1, and the LoD values are shown in **Table 5.1**. As with EIS results, the values of LoD were found to be lower when complexes **3** and complex **4** were used to modify the electrode for GCE-(**3**),(**4**)-aptamer compared to GCE-(**1**)-aptamer and GCE-(**2**)-aptamer and this is due to an asymmetrical substitution in the former. Comparing **3** with **4** alone and when

the aptamer is adsorbed in GCE-(**3**)-aptamer(ads) and GCE-(**4**)-aptamer(ads), respectively or covalently linked, the LoD is lower for **4**, most likely due to the bulkier substituent. The rest of the trends were outlined above for LoD determined using EIS.

5.2. Stability study

The stability of the probes was tested by running 50 consecutive DPV scans of PSA in the presence of 0.1 M KCl containing 1 mM $[Fe(CN)_6]^{3-/4-}$ prepared in a 30 mM phosphate buffer saline. The electrode GCE-EG-(**4**) (seq)-aptamer (ads) was used as an example. The stability of this electrode (**Fig. 5.2**) was characterized by a bit of change in current with scan number. The current increased slightly. Such high stability has been reported for aptasensors for PSA [94].

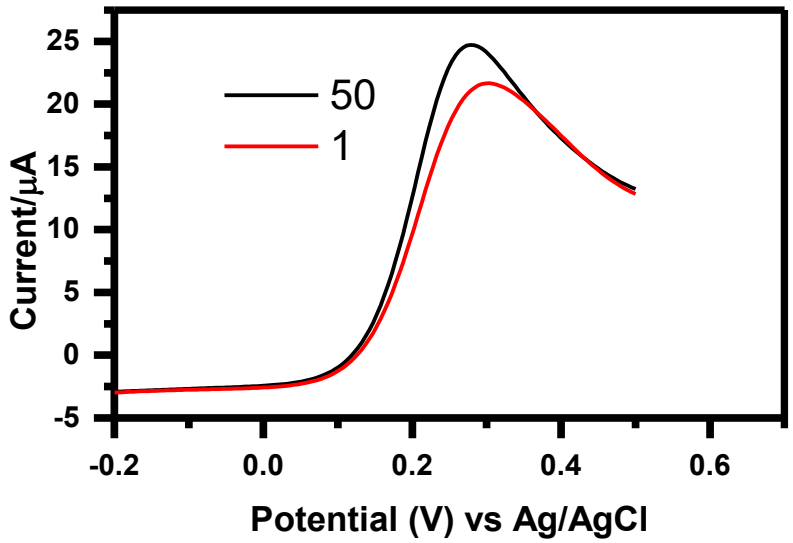

Figure 5.2: Differential pulse voltammograms of GCE-EG-(**4**) (seq)-aptamer (ads) in PSA solution of the concentration 1.5 pM of 50 cycles to test the electrode repeatability.

5.3. Interference studies

The blood serum contains different biological molecules such as proteins, enzymes, antibodies, and hormones [96]. The selectivity towards PSA was determined by performing DPV of PSA in the presence of possible interferents: glucose, cysteine, and bovine serum albumin (BSA). These interferences have been reported to detect PSA [94, 97]. The GCE-EG-**4**(seq)-aptamer(ads) electrode was chosen (**Fig. 5.3**) as a representative. The mixed solution method was used to mix the PSA with either glucose, cysteine, or BSA [98]. The concentrations of the interfering molecules that were added, were $\times 10^3$ more than that of PSA.

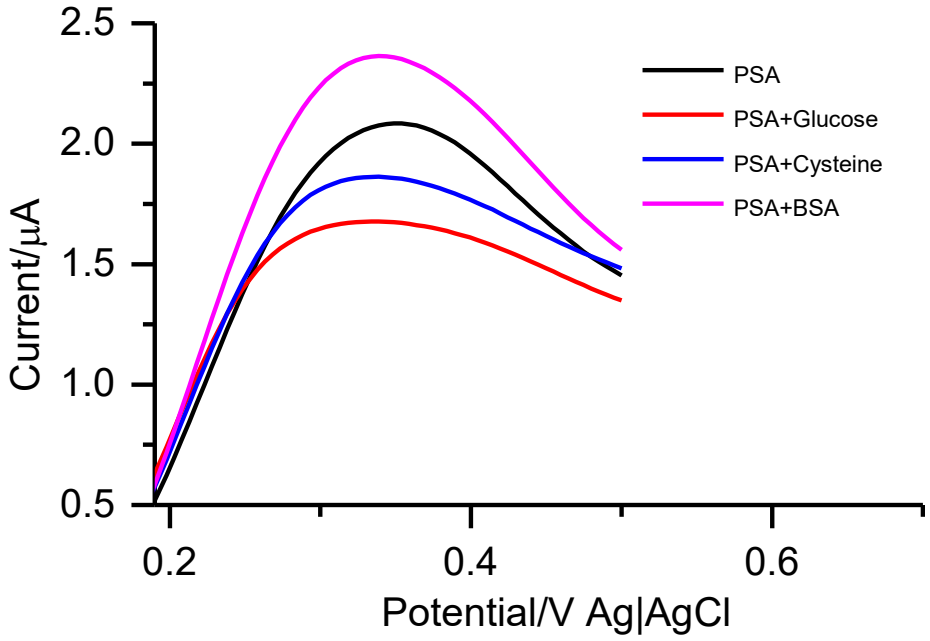

Figure 5.3: Differential Pulse Voltammograms (DPV) of GCE-EG-(**4**)(seq)-aptamer (ads) for PSA in the absence and presence of interferents (2nM of BSA, glucose and cysteine) in a PSA solution of concentration 1.5 pM. All in 1 M KCl containing 1 mM $[Fe(CN)_6]^{3-/4-}$ prepared in a 30 mM phosphate buffer saline.

The selective coefficient (K_{AMP}) of each interference was estimated using eq. 5.2.

$$K_{AMP} = (I_{MIXTURE} / I_{PSA}) \left({}^{[PSA]}/_{[Interference]} \right) \quad (5.2)$$

Where I_{PSA} and I_{mixure} are background corrected current of the PSA alone and with the interferences, respectively. The K_{AMP} values were estimated for all interferences (**Table 5.2**). This method for estimating selectivity coefficients has been employed before for biological systems [**99**]. A K_{AMP} value less than $\times 10^{-3}$ indicates a non-interfering species and a value greater than $\times 10^{-3}$ indicates an interfering species [**98**]. All the obtained K_{AMP} values were less than $\times 10^{-3}$, and this means even at higher concentrations of BSA, glucose, and cysteine, the sensor did not pick them, and so detecting PSA in a sample that contains these interferences will only allow for the PSA to be detected.

Table 5.2: K_{AMP} values of the interference mixed with 1.5 pM PSA solution.

Interferant	**K_{AMP}**
BSA	7.04×10^{-4}
Glucose	9.48×10^{-4}
Cysteine	3.80×10^{-4}

5.4. Sensor performance in real sample

The potential ability of the GCE-EG-(**4**)(seq)-aptamer(ads) electrode in real life was investigated in the blood human serum sample of a male. Before conducting the studies, the human serum was diluted with PBS buffer in a ratio of 1/500 to avoid the matrix effect [**100**]. Dilution factors in this range have been reported [**101**]. The human serum was spiked with various known concentrations of the PSA antigen, 1.0-2.0 pM (0.034-0.068 ng/mL) (**Table 5.3**). The percentage recoveries of the GCE-EG-(seq)(**4**)-

aptamer(ads) ranged from 82.4% to 93.4%. These percentages are within the range reported (81.4% to 116.0%) for other materials [102]. The relatively high recoveries are due to the synergistic effect of the CoPc and EG combinations and their role in detecting the PSA analyte.

Table 5.3: Percentage recoveries of different PSA concentrations in human serum (HS) of GCE-EG-(**4**)(seq)-aptamer(ads) electrode.

Concentration PSA (ng/mL)	**Concentration PSA in HS (ng/mL)**	**% recovery**
0.044	0.036	82.4
0.051	0.044	87.2
0.058	0.053	92.4
0.065	0.056	86.9

5.5. Summary of the Chapter

The sequentially modified electrodes of CoPc on EG in the presence of adsorbed aptamer gave the electrodes (GCE-EG-(**CoPc**)-aptamer. The covalent modification of an aptamer to complexes **3** and **4** resulted in lower LoD values than when the aptamer was adsorbed. The LoD values of the electrodes with covalently linked aptamer were lower than those reported in the literature in the presence of other nanomaterials, such as graphitic carbon nitride quantum dots. The presence of EG generally improved the LoD of CoPc. The GCE-EG-(**4**)(seq)-aptamer(ads) electrode was tested for selectivity in which BSA, glucose, and cysteine were used as the interferents. The obtained K_{AMP}

values were all lower than $\times 10^{-3}$, which shows that the above interferents were not picked by this work's biosensor, suggesting that no pretreatment was needed before detecting the PSA. The electrode also showed good stability after running 50 scans of the same electrode. The GCE-EG-(**4**)(seq)-aptamer(ads) in which a small change in current between scan 1 and scan 50 was observed. GCE-EG-(**4**)(seq)-aptamer(ads) electrode showed an excellent percentage recovery when human serum was spiked with different concentrations of PSA. Substituting the three complexes with various groups and employing EG with CoPc and covalent linking an aptamer to **3** and **4** was, therefore, successful in detecting the PSA.

Chapter 6: Conclusion and future aspects.

Conclusion and summary of the chapters discussed as well as future aspects are presented in this chapter.

6. Conclusions and Future aspects

6.1. Conclusion

The known phthalocyanines, cobalt tetra pyridyloxy Pc **(1)** and cobalt tetra acetamidophenoxy Pc **(2),** as well as novel phthalocyanines, cobalt tris(acetamidophenoxy)mono benzoic acid Pc **(3)** and Cobalt tris(acetamidophenoxy)mono propionic acid Pc **(4)** were successfully synthesized, and confirmed by various characterisation techniques such as UV-Vis and other methods discussed in this work. EG synthesized in this work was successfully confirmed using characterization techniques such as TGA and XRD etc. The spectroscopic characterization confirmed the successful conjugation of complexes **1**, **2**, **3** and **4** to EG. The electrochemical activity of CoPc complexes was improved in the presence of EG. In this work, symmetry played a significant role in electrocatalysis since the asymmetrical complexes **3** and **4** allowed for an aptamer to be either covalently linked (by the COOH group) or sequentially added onto these complexes, with the covalently attached aptamer electrodes performing better than all the electrodes. The lower limit of detection was obtained for asymmetrically substituted complexes in the presence of EG and covalently linked aptamer and was lower than the literature LoDs. The biosensor employed in this work showed weak interference effect using BSA, glucose, and cysteine as interferents. High stability, and good percentage recoveries in human serum studies of the electrode; GCE-EG-(**4**)(seq)-aptamer(ads) were also obtained in this work showing a success of employing this biosensor.

6.2. Future aspects

The most important factor of electrocatalytic activity of the electrode looked at in this work, is the material used as a modifier. The use of other dye materials such as porphyrins and boron-dypyrromethene (bodipy's) which are synthesized in the lab can be used. Various nanomaterials including EG and those similar to EG, such as graphene quantum dots, pristine and functionalized, conjugated with complexes, will be used as modifiers. Biosensors involve a wide range of biorecognition elements, such as antibodies, which can also be used and compared to the electrodes with an aptamer used in this work when CoPc and EG used or other dyes and other nanomaterials are used.

References

[1] G. De la Torre, T. Torres, Synthetic advances in phthalocyanine chemistry , J. Porphyr. Phthalocyanines 6 (**2002**) 281-282**.**

[2] G. de la Torre, C.G. Claessens, and T. Torres, Phthalocyanines: The need for selective synthetic approaches, Eur. J. Org. Chem. 16 (**2000**) 2821-2830.

[3] M. Hanack, M. Lang, Conducting stacked metallophthalocyanines and related compounds. Adv. Mater. 6 (**1994**) 819–833.

[4] M.N. Yaraşir, A. Aytekin, M. Kandaz, O. Güney, Selective recognition of palladium based on functional mono phthalocyanines; synthesis, characterization and photophysical properties J. Lumin. 177 (**2016**) 342-348.

[5] M. Kandaz, M.N. Yaraşir, T. Güney, A. Koca, Both alcohol and halogenated solvents soluble soft-metal sensor functional phthalocyanines: synthesis, electrochemistry, spectroelectrochemistry, J. Porphyr. Phthalocyanines 13 (**2009)** 712-721.

[6] M.N. Yaraşir, M. Kandaz, A. Koca, Amido functional phthalocyanines as metal ion sensor; synthesis, characterization, spectroscopy, electrochemistry, in-situ spectroelectrochemistry, Inorg. Chim. Acta. 365 (**2011**) 256-263.

[7] T. Komatsu, K. Ohta, T. Fujimoto, I. Yamamoto, Chromic materials. Part 1. — Liquid-crystalline behaviour and electrochromism in bis (octakis-n-alkylphthalocyaninato) lutetium (III) complexes, J. Mater. Chem. 4 (**1994**) 533-536.

[8] M.G. Walter, B.A. Rudine, C.C. Wamser, Porphyrins and phthalocyanines in solar photovoltaic cells, J. Porphyr Phthalocyanines 14 (**2010**) 759-792.

[9] G.G. Roberts, M.C. Petty, S. Baker, M.T. Fowler, N.J. Thomas, Electronic devices incorporating stable phthalocyanine Langmuir-Blodgett films, Thin Solid Films 132 (**1985**) 113-123.

[10] G. De La Torre, P. Vázquez, F. Agullo-Lopez, T. Torres, Role of structural factors in the nonlinear optical properties of phthalocyanines and related compounds, Chem. Rev. 104 (**2004**) 3723-3750.

[11] J.D. Miller, E.D. Baron, H. Scull, A. Hsia, J.C. Berlin, T. McCormick, V. Colussi, M.E. Kenney, K.D. Cooper, N.L. Oleinick, Photodynamic therapy with the phthalocyanine photosensitizer Pc 4: the case experience with preclinical mechanistic and early clinical–translational studies, Toxicol. Appl. Pharmacol. 224 (**2007**) 290-299.

[12] J. Garcia, A. Gonzalez, A. Gouloumis, E.M. Maya, M.D. Perez, B.D. Rey, P. Vazquez, T. Torres, Phthalocyanines and related compounds: subunits for the preparation of molecular materials, Turk. J. Chem. 22(**1998**) 23-32.

[13] Y.H. Lu, R.G. Reddy, The electrochemical behavior of cobalt phthalocyanine/platinum as methanol-resistant oxygen- reduction electrocatalysts for DMFC. Electrochim. Acta. 52 (**2007**) 2562-2569.

[14] B. Mu, A. Wang, Fabrication and Applications of Carbon/Clay Mineral Nanocomposites, in: Nanonaterials from Clay Minerals, A. Wang, W. Wang (eds), Elsevier, Amsterdam: The Netherlands (**2019**) 537-587.

[15] M. Gouterman, Optical spectra and electronic structure of porphyrins and related rings, David Dolphin (eds), Academic press, New York (**1978)** 12-13.

[16] J. Mack, N. Kobayashi, Low symmetry phthalocyanines and their analogues, Chem. Rev. 111 (**2011**) 281–321.

[17] V. N. Nemykin, E. A. Lukyanets, Synthesis of substituted phthalocyanines, Arkivoc (**2010)** 136–208.

[18] N.B. McKeown, Phthalocyanine-containing polymers, J. Mater. Chem. 10 (**2000**)1979-1995.

[19] D. Gounden, G.N. Ngubeni, M.S. Louzada, S. Khene, J. Britton, N. Nombona, Synthesis, spectroscopic and DFT characterization of 4 β-(4-tert-butylphenoxy) phthalocyanine positional isomers for non-linear optical absorption, S. Afr. J. Chem. 70 (**2017**) 49-59.

[20] K. A. Bello, I. A Bello, Some observations on the visible absorption spectra and stability properties of the silicon phthalocyanine system, Dyes Pigm. 35 (**1997**) 261-267.

[21] İ. Özçeşmeci, A. Demir, D. Akyüz, A. Koca, A. Gül, Electrocatalytic hydrogen evolution reaction with a supramolecular cobalt (II) phthalocyanine carrying four cobaloxime moieties, Inorg. Chim. Acta. 466 (**2017**) 591-598.

[22] N. Nnaji, P. Sen, T. Nyokong, Aluminum corrosion retardation properties of acetamidophenoxy phthalocyanines: Effect of central metal. J. Mol. Struct. 1242 (**2021**) 130806**.**

[23] S. Centane, E.K. Sekhosana, R. Matshitse, T. Nyokong, Electrocatalytic activity of a push-pull phthalocyanine in the presence of reduced and amino functionalized graphene quantum dots towards the electrooxidation of hydrazine, J. Electroanal. Chem. 820 (**2018**) 146-160.

[24] D.D.L. Chung, A review of exfoliated graphite J. Mater. Sci. 51(**2016)** 554-568.

[25] H. Terrones, M. Terrones, JL. Moran-López, Curved nanomaterials, Current Science 81 (**2001**) 1011-1029.

[26] A. Callard, J. F Marche, G. Furdin, Modelling of exfoliated graphite, Prog.Mater. Sci. 50 (**2005**) 93-179.

[27] Y.Li, Y. Lu, P. Adelhelm, M.M. Titirici, Y.S. Hu, Intercalation Chemistry of Graphite: Alkali Metal Ions and Beyond. Chem. Soc. Rev. 48 (**2019**) 4655–4687.

[28] J. Xu, Y. Dou, Z. Wei, J. Ma, Y. Deng, Y. Li, H. Liu, S. Dou, Recent Progress in Graphite Intercalation Compounds for Rechargeable Metal (Li, Na, K, Al)-Ion Batteries. Adv. Sci. 4 (**2017**) 1700146.

[29] A. O. Idris, B. O. Orimolade, M. Potlako, U. Feleni, T. T. I. Nkambule, B. B. Mamba, Exfoliated Graphite: A Surface, Renewed Electrode for Environmental Applications, Front. Sens. 3 (**2022**) 861965. doi: 10.3389/fsens.2022.86196.

[30] A. Yamuna, P. Sundaresan, S.-M. Chen, Ethylcellulose assisted exfoliation of graphite by the ultrasound emulsification: An application in electrochemical acebutolol sensor, Ultrason. Sonochem. 59 (**2019**) 104720.

[31] R. V. Jagadeesh, V. Lakshminarayanan, Enhanced electrocatalytic activity of Pd and Pd-polyaniline nanoparticles on electrochemically exfoliated graphite sheets, Appl. Catal. B. 251 (**2019**) 25–36.

[32] S. Maree and T. Nyokong, Electrocatalytic behaviour of substituted cobalt phthalocyanines towards the oxidation of cysteine, J. Electroanal. Chem. 492 (**2000**) 120-127.

[33] E. Demir, H. Silah, B. Uslu, Phthalocyanine modified electrodes in electrochemical analysis, Crit. Rev. Anal. Chem. 52 (**2020**) 425-461.

[34] T. Nyokong, S. Khene, in Modification of electrode surfaces with metallo phthalocyanine nanomaterial hybrids in: Electrochemistry of N4 macrocyclic metal complexes, J.H. Zagal, F. Bedioui (eds), Springer, New York (**2006**) 225-276.

[35] M.P. Somashekarappa, S. Sampath Sol–gel derived, silicate-phthalocyanine functionalized exfoliated graphite based composite electrodes, Anal. Chim. Acta. 503 (**2004**) 195–201.

[36] L. Saikam, P. Arthi, B. Senthil, M. Shanmugam, A Review on Exfoliated Graphite: Synthesis and Applications. Inorg. Chem. Commun. 152 (**2023**) 110685.

[37] X. Van Heerden, H. Badenhorst, The influence of three different intercalation techniques on the microstructure of exfoliated graphite, Carbon 88 (**2015**) 173–184.

[38] Y. Chen, R. Luo, S. Li et al., “Preparation of highly–expandable graphite using waste liquid propellants of nitric-27S as one of intercalating agents, Carbon 50 (**2012**) 2063.

[39] H. M. A. Asghar, S. N. Hussain, H. Sattar, N. W. Brown, E. P. L. Roberts, Environmentally friendly preparation of exfoliated graphite, J. Ind. Eng. Chem. 20 (**2014**) 1936–1941.

[40] J. He, L. Song, H. Yang, X. Ren, L. Xing, 2017. Preparation of sulfur-free exfoliated graphite by a two-step intercalation process and its application for adsorption of oils. J. Chem. 2017 (**2017**) 1.

[41] M. Inagaki, R. Tashiro, Y.-I. Washino, M. Toyoda, Exfoliation process of graphite via intercalation compounds with sulfuric acid, J. Phys. Chem. Solids. 65 (**2004**) 133–137.

[42] R. Bissessur, S. F. Scully, Intercalation of solid polymer electrolytes into graphite oxide, Solid State Ion 178 (**2007**) 877–882.

[43] J.P. Mafa, N. Mabuba, O.A. Arotiba, An exfoliated graphite based electrochemical sensor for As (III) in water. Electroanalysis 28 (**2016**) 1462-1469.

[44] D.P. Masemola, P.J. Mafa, H. Nyoni, B.B. Mamba, T.A. Msagati, Gold nanoparticles modified exfoliated graphite electrode as electrochemical sensor in the determination of psychoactive drug. J. Environ. Sci. Health 55 (**2020**) 455-461.

[45] T.R. Silva, A. Smaniotto, I.C. Vieira, Exfoliated graphite nanoplatelets and gold nanoparticles based electrochemical sensor for determination of levodopa, J Solid State Electrochem. 22 (**2018**) 1277-1287.

[46] T. Ndlovu, B.B. Mamba, S. Sampath, R.W. Krause, O.A. Arotiba, Voltammetric detection of arsenic on a bismuth modified exfoliated graphite electrode, Electrochim. Acta. 128 (**2014**) 48-53.

[47] A. Jimana, M.G. Peleyeju, L. Tshwenya, K. Pillay, O.A. Arotiba, Voltammetric analysis of As (III) at a cobalt nanoparticles/reduced graphene oxide modified exfoliated graphite electrode, Int. J. Electrochem. Sci. 13(**2018**) 10127-10140.

[48] T. Ndlovu, O.A. Arotiba, S. Sampath, R.W. Krause, B.B. Mamba, Electroanalysis of copper as a heavy metal pollutant in water using cobalt oxide modified exfoliated graphite electrode, Phys. Chem. Earth 50 (**2012**) 127-131.

[49] T. Ndlovu, O.A. Arotiba, S. Sampath, R.W. Krause, B.B. Mamba, Electrochemical detection and removal of lead in water using poly (propylene imine) modified re-compressed exfoliated graphite electrodes. J. Solid State Electrochem. 41 (**2011**) 1389-1396.

[50] B.O. Orimolade, O.A. Arotiba, An exfoliated graphite-bismuth vanadate composite photoanode for the photoelectrochemical degradation of acid orange 7 dye, Electrocatalysis 10 (**2019**) 429-435.

[51] B.O. Orimolade, B.A. Koiki, B.N. Zwane, G.M. Peleyeju, N. Mabuba, O.A. Arotiba, Interrogating solar photoelectrocatalysis on an exfoliated graphite–BiVO 4/ZnO composite electrode towards water treatment. RSC advances 9 (**2019**) 16586-16595.

[52] E.H. Umukoro, M.G. Peleyeju, J.C. Ngila, O.A. Arotiba, Towards wastewater treatment: Photo-assisted electrochemical degradation of 2-nitrophenol and

orange II dye at a tungsten trioxide-exfoliated graphite composite electrode, J. Chem. Eng. 317(**2017**) 290-301.

[53] O.M. Ama, O.A. Arotiba, Exfoliated graphite/titanium dioxide for enhanced photoelectrochemical degradation of methylene blue dye under simulated visible light irradiation, J. Electroanal. Chem. 803 (**2017**) 157-164.

[54] B. Ntsendwana, S. Sampath, B.B. Mamba, O.S. Oluwafemi, O.A. Arotiba, Photoelectrochemical degradation of eosin yellowish dye on exfoliated graphite–ZnO nanocomposite electrode, J. Mater. Sci.: Mater. Electron. 27 (**2016**) 592-598.

[55] P.J. Mafa, B.B. Mamba, A.T. Kuvarega, Photoelectrocatalytic evaluation of EG-CeO2 photoanode on degradation of 2, 4-dichlorophenol, Sol. Energy Mater Sol. Cells 208 (**2020**) 110416.

[56] O.M. Ama, N. Kumar, F.V. Adams, S.S. Ray, Efficient and cost-effective photoelectrochemical degradation of dyes in wastewater over an exfoliated graphite-MoO 3 nanocomposite electrode Electrocatalysis 9 (**2018**) 623-631.

[57] O.M. Ama, A.W. Wilson, S.S. Ray, Photoelectrochemical degradation of methylene blue dye under visible light irradiation using EG/Ag-ZrO2 nanocomposite electrodes, Int. J. Electrochem. Sci. 14 (**2019**) 9982-10001.

[58] P.J. Mafa, R. Patala, B.B. Mamba, D. Liu, J. Gui, A.T. Kuvarega, Plasmonic Ag3PO4/EG photoanode for visible light-driven photoelectrocatalytic degradation of diuretic drug, J. Chem. Eng. 393 (**2020**) 124804.

[59] P. Mehrotra, Biosensors and their applications–A review, J. Oral Biol. Cran. Res. 6 (**2016**) 153-159.

[60] Z. Zhang, J. Zhou, X. Du, Electrochemical biosensors for detection of foodborne pathogens, Micromachines 10 (**2019**) 222.

[61] S.R. Nxele, D.O. Oluwole, T. Nyokong, Electrocatalytic activity of a push pull Co (II) phthalocyanine in the presence of graphitic carbon nitride quantum dots, Electrochimica Acta 326(**2019**) 134978.

[62] H. Lilja, D. Ulmert, A.J. Vickers, Prostate-specific antigen and prostate cancer: prediction, detection and monitoring, Nat. Rev. Cancer 8 (**2008**) 268-278.

[63] Z. Akbari jonous, J.S. Shayeh, F. Yazdian, A. Yadegari, M. Hashemi, M. Omidi, An electrochemical biosensor for prostate cancer biomarker detection using graphene oxide–gold nanostructures, Eng. Life Sci. 19 (**2019**) 206-216.

[64] B. Qu, X. Chu, G. Shen, R. Yu, A novel electrochemical immunosensor based on colabeled silica nanoparticles for determination of total prostate specific antigen in human serum, Talanta 76 (**2008**) 785-790.

[65] L. Huang, G. Reekmans, D. Saerens, J.M. Friedt, F. Frederix, L. Francis, S. Muyldermans, A. Campitelli, C. Van Hoof, Prostate-specific antigen immunosensing based on mixed self-assembled monolayers, camel antibodies and colloidal gold enhanced sandwich assays, Biosens. Bioelectron. 21(**2005**) 483-490.

[66] S.R. Nxele, T. Nyokong, The electrochemical detection of prostate specific antigen on glassy carbon electrode modified with combinations of graphene quantum dots, cobalt phthalocyanine and an aptamer. J. Inorg. Biochem. 221 (**2021**) 111462.

[67] P. Karami, H. Bagheri, M. Johari-Ahar, H. Khoshsafar, F. Arduini, A. Afkhami, Dual-modality impedimetric immunosensor for early detection of prostate-specific antigen and myoglobin markers based on antibody-molecularly imprinted polymer, Talanta 202 (**2019**) 111–122.

[68] J-M. Moon, Y.H. Kim, Y. Cho, A nanowire-based label-free immunosensor: Direct incorporation of a PSA antibody in electropolymerized polypyrrole, Biosens. Bioelectron. 57 (**2014**) 157-161.

[69] S.Y. Toh, M. Citartan, S.C.B. Gopinath, T.-H. Tang, Aptamers as a replacement for antibodies in enzyme-linked immunosorbent assay, Biosens. Bioelectron. 64 (**2015**) 392–403.

[70] Z. Xiao, J. Frieder, B.A. Teply, O. Farokhzad, Aptamer conjugates: Emerging delivery platforms for targeted cancer therapy. In Drug Delivery Oncology: From Basic Research Cancer Therapy, Z. Xiao, J. Frieder, A.B. Teply, C.O. Farokzad (eds), Wiley: Weinheim, Germany (**2012**) 1263–1281.

[71] K. Park, S.A. Tomlins, K.M. Mudaliar, Y.L. Chiu, R. Esgueva, R. Mehra, K. Suleman, S. Varambally, J.C. Brenner, T. MacDonald, A. Srivastava, Antibody-based detection of ERG rearrangement-positive prostate cancer, Neoplasia 12 (**2010**) 590-591.

[72] A. Chen, S. Yang, Replacing antibodies with aptamers in lateral flow immunoassay, Biosens. Bioelectron. 71 (**2015**) 230- 242.

[73] S. R. Nxele, T. Nyokong, The effects of quantum dots composition and structure in combination with cobalt phthalocyanine and an Aptamer on the electrochemical detection of prostate specific antigen, Dyes Pigm. 192 (**2021**) 109407.

[74] S.R. Nxele, R. Nkhahle, T. Nyokong, The composites of asymmetric Co phthalocyanines-graphitic carbon nitride quantum dots-aptamer as specific electrochemical sensors for the detection of prostate specific antigen: Effects of ring substituents, J. Electroanal. Chem. 900 (**2021**) 115730.

[75] S.R. Nxele, R. Nkhahle, T. Nyokong, The synergistic effects of coupling Au nanoparticles with an alkynyl Co (II) phthalocyanine on the detection of prostate specific antigen, Talanta 237 (**2022**)122948.

[76] Y.J. Li, M.J. Ma, G.Yin, Y. Kong, J.J. Zhu, Phthalocyanine-Sensitized Graphene–CdS Nanocomposites: An Enhanced Photoelectrochemical Immunosensing Platform, Chem. Eur. J. 19 (**2013**) 4496-4505.

[77] M. S. Agırtas, M. S. Izgi, Synthesis and characterization of new metal-lophthalocyanines with four phenoxyacetamide units, J. Mol. Struct. 927 (**2009**) 126–128, doi: 10.1016/j.molstruc.2009.03.011.

[78] H. Kliesch, A. Weitemeyer, S. Müller, D. W¨ohrle, Synthesis of phthalocyanines with one sulfonic acid, carboxylic acid, or amino group, Liebigs Ann. Chem. 7 (**1995**) 1269–1273.

[79] E. Dube, N. Nwaji, D.O. Oluwole, J. Mack, T. Nyokong, Investigation of photophysicochemical properties of zinc phthalocyanines conjugated to metallic nanoparticles. J. Photochem. Photobiol. A: Chem. 349 (**2017**) 148.

[80] L.S Mpeta, S.S. Gwebu, O.A. Arotiba, N.W. Maxakato, Methanol oxidation in alkaline media with Pt-Au/fMWCNTs and Pt-Pd/fMWCNTs electrocatalysts on an exfoliated graphite electrode, Electrocatalysis 10 (**2019**) 672-679.

[81] A. Maringa, E. Antunes, T. Nyokong, Electrochemical behaviour of gold nanoparticles and Co tetraaminophthalocyanine on glassy carbon electrode, Electrochim. Acta. 121 (**2014**) 93-101.

[82] W. Zhao, W. Chiuman, J. C. F. Lam, S. A. McManus, W. Chen, Y. Cui, R. Pelton, Mi. A. Brook, Y. Li, DNA Aptamer Folding on Gold Nanoparticles: From Colloid Chemistry to Biosensors J. Am. Chem. Soc. 130 (**2008)** 3610-3618.

[83] J. Rusanova, M. Pilkington, S. Decurtins, A novel fully conjugated phenanthroline-appended phthalocyanine: Synthesis and characterisation, Chem. Commun. 19 (**2002**) 2236–2237, https://doi.org/10.1039/B206973C.

[84] G. Fomo, N. Nwaji, T. Nyokong, Low symmetric metallophthalocyanine modified electrode via clickchemistry for simultaneous detection of heavy metals, J. Electroanal. Chem. 813 (**2018**) 66.

[85] G. Balakrishnan, A. V. Soldatova, P. J. Reid, T.G. Spiro, Ultrafast Charge Transfer in Nickel Phthalocyanine Probed by Femtosecond Raman-Induced Kerr Effect Spectroscopy, J. Am. Chem. Soc. 136 (**2014**) 8746−8754.

[86] W.F. Smith, Principles of materials science and engineering, McGraw-Hill, New York, (**1990)** p. 724.

[87] G. Chen, W. Weng, D. Wu, W. Weng and C. Wu**,** PMMA/graphite nanosheets composite and its conducting properties, Eur. Polym. J. 39 (**2003**) 2329-2335.

[88] N.B. Hoang, T.T. Nguyen, T.S. Nguyen, T.P.Q. Bui, L.G. Bach, The application of expanded graphite fabricated by microwave method to eliminate organic dyes in aqueous solution, Cogent Eng. 6(**2019**)1584939.

[89] D.J. Vaughan, Graphite to Graphene: From a Mineral to an Advanced Technological Material, Elements 15 (**2019**) 215-216.

[90] Z. D. Liu, H. X. Zhao, C. Z. Huang, Obstruction of photoinduced electron transfer from excited porphyrin to graphene oxide: a fluorescence turn-on sensing platform for iron (III) ions, PLoS One 12 (**2012**) 50367.

[91] P.L. Yap, S. Kabiri, D.N.H. Tran, D. Losic, Multifunctional binding chemistry on modified graphene composite for selective and highly efficient adsorption of mercury, ACS Appl. Mater. Interfaces 11 (**2019**) 6350–6362.

[92] A Y. Lee, K. Yang, N. D. Anh, C. Park, S. Mi Lee, T. G. Lee, M. Seok Jeong, Raman study of D* band in graphene oxide and its correlation with reduction, Appl. Surf. Sci. 536 (**2021**) 147990.

[93] F. J. Rawson, A. J. Downard, and K. H. Baronian, Electrochemical detection of intracellular and cell membrane redox systems in Saccharomyces cerevisiae. Sci. Rep. 4 (**2014**) 9.

[94] M. Srivastava, N. R. Nirala, S. K. Srivastava, R. Prakash, A comparative Study of Aptasensor Vs Immunosensor for Label-Free PSA Cancer Detection on GQDs-AuNRs Modified Screen-Printed Electrodes, Scient. Rep. 8 (**2018**) 1923, DOI:10.1038/s41598-018-19733-z.

[95] F.S. Tabar, M. Pourmadadi, H. Rashedi, F. Yazdian, Design of Electrochemical Nanobiosensor in the Diagnosis of Prostate Specific Antigen (PSA) Using Nanostructures. In Proceedings of the 2020 27th National and 5th International Iranian Conference on Biomedical Engineering (ICBME), Tehran, Iran, 26–27 November **2020**, p. 35–40.

[96] A. Rahi, N. Sattarahmady, H. Heli, Label-free electrochemical aptasensing of the human prostate-specific antigen using gold nanospears, Talanta 156 (**2016**) 218-224.

[97] H. L. Tran, W. Darmanto, R.-A. Doong, Electrochemical immunosensor for ultra-sensitive detection of attomolar prostate specific antigen with sulfur-doped graphene quantum dot@gold nanostar as the probe, Electrochim. Acta. 389 (**2021**) 138700.

[98] R.I. Stefan, J.F. van Staden, H.Y Aboul-Enien, Electrochemical sensors in Bioanalysis, Marcel Dekker, New York, **2001**, 65.

[99] J. Wang, L. Chen, Selectivity coefficients of class-selective enzyme electrodes, Biosens. & Bioelectron. 11 (**1996**) 751-756.

[100] S. Rodriguez-Mozaz, M.J. Lopez de Alda, D. Barceló, Biosensors as useful tools for environmental analysis and monitoring, Anal.Bioanal.Chem.386 (**2006**) 1025-1041.

[101] M. Cortese, M. R. Gigliobianco, F. Magnoni, R. Censi, P. Di Martino, Compensate for or Minimize Matrix Effects? Strategies for Overcoming Matrix Effects in Liquid Chromatography-Mass Spectrometry Technique: A Tutorial Review, Molecules 25 (**2020**) 3047; doi:10.3390/molecules25133047.

[102] J.-T. Cao, J.-J. Yang, L.-Z. Zhao, Y.-L. Wang, H. Wang, Y. M. Liu, S.-H. Ma, Graphene oxide@gold nanorods-based multiple-assisted electrochemiluminescence signal amplification strategy for sensitive detection of prostate specific antigen, Biosens. Bioelectron. 99 (**2018)** 92–98.

Appendix

Statistically analysis data of cobalt tetra pyridiloxy Pc(1)

Yield: 60.4 mg, 15.9 % (w/w); UV/Vis (DMF): λ_{max}/nm (log Ɛ): 668 (4.14), 609 (3.72), 325 (4.04). IR [(KBr), v_{max}/cm^{-1}]: 746 (aromatic C-H_{str}), 1089 (C-O-C), 1225 (O-C_{str}), 1401 (-OH_{bend}), 1503 (C-H), 1660 (C=O), 3053 (C=H). Anal. calc. for $C_{63}H_{49}CoN_{11}O_9$•$4H_2O$: C, 61.7; N, 12.6. Found: C, 60.4; N, 12.3. MS (MALDI-TOF) (m/z): calc.: 1154.24 amu; found: 1155.82 amu $[M+H]^+$.

Statistically analysis data of cobalt tetra acetamidophenoxy Pc (2)

Yield: 49.7 mg, 13.0 % (w/w); UV/Vis (DMF): λ_{max}/nm (log Ɛ): 667 (4.42), 610 (4.08), 324 (4.41). IR [(KBr), v_{max}/cm^{-1}]: 746 (aromatic C-H_{str}), 1091 (C-O-C), 1229 (O-C_{str}), 1403 (-OH_{bend}), 1503 (C-H), 1656 (C=O),2936 (aliphatic C-H_{str}), 3051 (C=H). Anal. calc. for $C_{65}H_{45}CoN_{11}O_9$• $5H_2O$: C, 61.3; N, 12.1. Found: C, 61.3; N; 12.2. MS (MALDI-TOF) (m/z): calc.: 1182.27 amu; found: 1182.76 amu $[M]^+$.

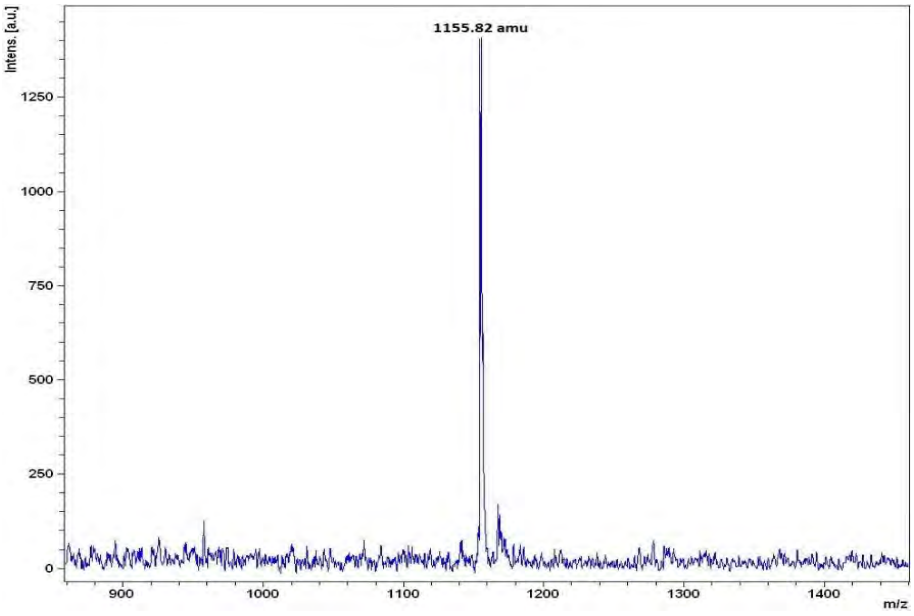

Figure A1: Mass spectra for complex **3**.

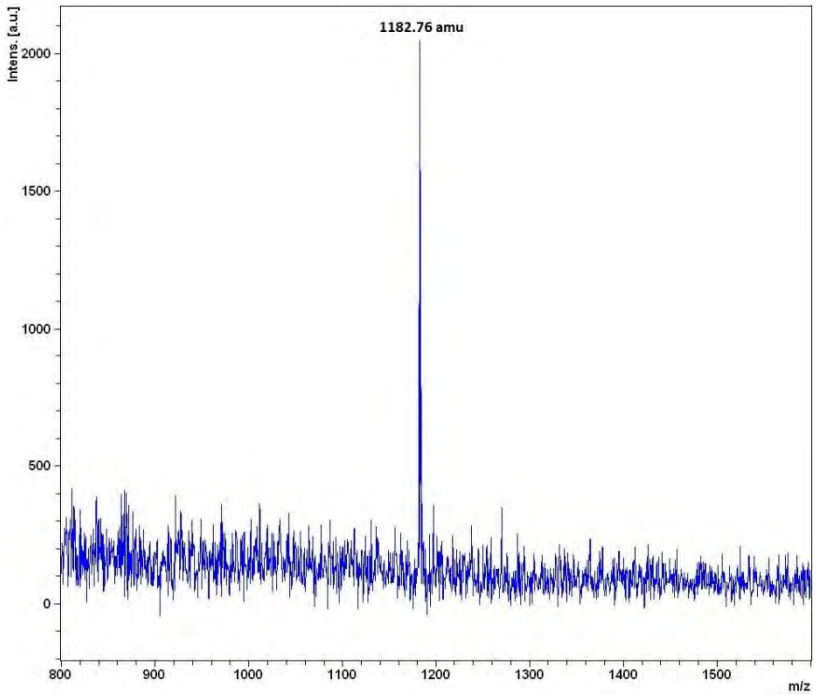

Figure A2: Mass spectra for complex **4**.

.